SOUND AND WAKE CHARACTERISTICS GENERATED BY FLOW PAST A TRIANGULAR CYLINDER AT VARIOUS INCIDENT ANGLES

THANAKORN CHANTHANASARO

**A THESIS SUBMITTED IN PARTIAL FULFILLMENT
OF THE REQUIREMENTS FOR THE DEGREE OF
MASTER OF SCIENCE (PHYSICS)
FACULTY OF GRADUATE STUDIES
MAHIDOL UNIVERSITY
2020**

Thesis
entitled

SOUND AND WAKE CHARACTERISTICS GENERATED BY FLOW PAST A TRIANGULAR CYLINDER AT VARIOUS INCIDENT ANGLES

.....
Mr. Thanakorn Chanthanasaro
Candidate

.....
Chaiwoot Boonyasiriwat,
Ph.D. (Computing)
Major advisor

.....
Asst. Prof. Narumon Emarat,
Ph.D. (Applied Physics)
Co-advisor

.....
Assoc. Prof. Michael Anthony Allen,
Ph.D. (Physics)
Co-advisor

.....
Prof. Patcharee Lertrit,
M.D., Ph.D. (Biochemistry)
Dean
Faculty of Graduate Studies
Mahidol University

.....
Assoc. Prof. Kittiwit Matan,
Ph.D. (Physics)
Program Director
Master of Science Program in Physics
(International Program)
Faculty of Science
Mahidol University

Thesis
entitled

SOUND AND WAKE CHARACTERISTICS GENERATED BY FLOW PAST A TRIANGULAR CYLINDER AT VARIOUS INCIDENT ANGLES

was submitted to the Faculty of Graduate Studies, Mahidol University
for the degree of Master of Science (Physics)
on
November 25, 2020

.....
Mr. Thanakorn Chanthanasaro
Candidate

.....
Asst. Prof. Nirut Pussadee,
Ph.D. (Physics)
Chair

.....
Chaiwoot Boonyasiriwat,
Ph.D. (Computing)
Member

.....
Assoc. Prof. Michael Antony Allen,
Ph.D. (Physics)
Member

.....
Asst. Prof. Narumon Emarat,
Ph.D. (Applied Physics)
Member

.....
Prof. Patcharee Lertrit,
M.D., Ph.D. (Biochemistry)
Dean
Faculty of Graduate Studies
Mahidol University

.....
Assoc. Prof. Palangpon Kongsaeree,
Ph.D. (Chemistry)
Dean
Faculty of Science
Mahidol University

ACKNOWLEDGEMENTS

Firstly, I would like to thank my advisor, Dr. Chaiwoot Boonyasiriwat, for his useful guidance and many suggestions for my thesis. Furthermore, I would also like to thank Asst. Prof. Dr. Narumon Emarat and Assoc. Prof. Dr. Michael Antony Allen for a lot of helpful advice and valuable suggestions.

Second, I thank the Development and Promotion of Science and Technology Talents Project (DPST) scholarship for the opportunity and the financial support during many years of my academic study.

Lastly, I thank my friends, the juniors, the staffs at the physics department, my family, and myself also for both continuous encouragement and financial support during this rough time. Without them, this thesis could not be completed.

Thanakorn Chanthanasaro

SOUND AND WAKE CHARACTERISTICS GENERATED BY FLOW PAST A TRIANGULAR CYLINDER AT VARIOUS INCIDENT ANGLES

THANAKORN CHANTHANASARO 5836049 SCPY/M

M.Sc. (PHYSICS)

THESIS ADVISORY COMMITTEE : CHAIWOOT BOONYASIRIWAT, Ph.D., NARUMON EMARAT, Ph.D., MICHAEL ANTHONY ALLEN, Ph.D.

ABSTRACT

Characteristics of sound and wakes generated by flow past a triangular cylinder with Mach number 0.3 at various incident angles are studied by numerically solving the compressible Navier-Stokes equations using OpenFOAM. The Reynolds number in this study is varied from 140 to 180. The mean lift coefficient is zero when the cylinder is symmetric and has a maximum when the incident angle is approximately 30°. The mean drag coefficient varies when the incident angle increases. The root mean square of the lift coefficient increases as the incident angle increases, while that of the drag coefficient is highest at an incident angle of around 36°. When the incident angle is small, the Strouhal number has the value of around 0.21. As an incident angle increases, the Strouhal number increases by approximately 1.5%. When the incident angle exceeds 24°, the Strouhal number drops to its minimum by 25% at an incident angle of 54° then slightly goes up by 4.5% at an incident angle of 60°. Increasing the Reynolds number does not significantly affect the trends of the vortex shedding frequency and the root mean square of the force coefficients. The root mean square of the pressure wave in the transverse and the upstream directions vary in the same manner as those of the lift and drag coefficients, respectively. At an incident angle of 60°, the root mean square of the pressure wave in the transverse direction increases by 115% compared to when the incident angle is small. While that in the upstream direction increases by 159% at an incident angle of 36° and decreases afterwards by 76% at an incident angle of 60°. The nearest vortex streets behind the cylinder are observed to be either the Bénard-von Kármán vortex street or the P+S-like wake. Both types of wake turn into the secondary vortex street while advected downstream.

KEY WORDS: AEROACOUSTICS/ COMPUTATIONAL FLUID DYNAMICS

70 pages

CONTENTS

CONTENTS (cont.)

LIST OF TABLES

LIST OF FIGURES

LIST OF FIGURES (cont.)

CHAPTER I
INTRODUCTION

1.1 Introduction and a literature review

Aeroacoustics is the study of noise induced by the fluid motion or aerodynamic forces interacting with surfaces. The sources of aerodynamics noise can be from the turbulent motion of the fluid, the fluctuating mass, or the fluctuating forces exerting on the surfaces if there are surfaces present in the flow field (Lighthill, 1952; Curle, 1955). At a low Mach number, Curle (1955) showed that the sound generated by the fluctuation of forces on the surfaces dominates the sound generated from other sources. For flow past a cylinder at a very low Reynolds number, it is already known that the flow is steady and nothing changes with advancing time. Beyond a specific Reynolds number, the flow becomes unsteady and the vortex shedding will take the place of the steady flow. This vortex shedding phenomenon gives rise to the fluctuation of lift and drag forces acting on the cylinder. For flow past a simple-shape bluff body, a body that can separate the flow, such as a circular cylinder at a low Reynolds number, the time variation of lift and drag forces has the form of a sinusoidal wave. When the vortex shedding is from the upper side of the circular cylinder, the lift coefficient takes its maximum. On the other hand, when the vortex shedding is from the lower side of the cylinder, the lift coefficient takes its minimum. For this reason, the fluctuation frequency of the lift force is then equal to the frequency of vortex shedding. This vortex shedding frequency is equivalent to the Strouhal number describing an oscillation in the flow and having the value slightly varying around 0.2 over a large range of Reynolds number.

The sound induced by the periodic vortex shedding from flow past cylinders, sometimes called Aeolian tone, has been experimentally and computationally studied for many decades (Blevins, 1983; Fujita et al., 1998; Doolan, 2009; Fujita, 2010; Lysenko, Ertesvåg, and Rian; 2014; Oguma, and Fujisawa; 2016). Inoue and

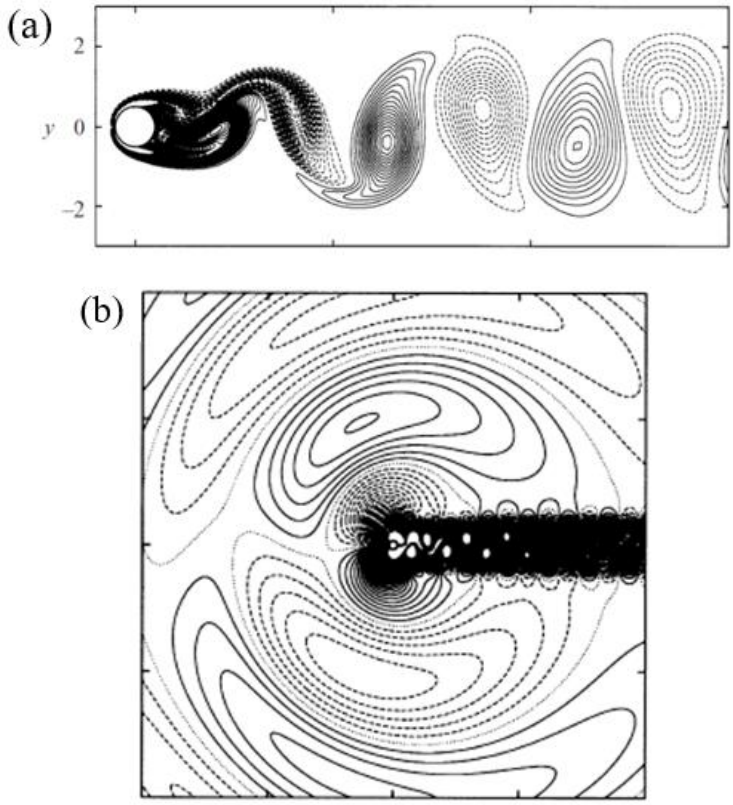

Figure 1.1 (a) The contour of vorticity when the vortex is shedding from the upper side of the circular cylinder. (b) The negative and positive pressure pulses are generated at the upper and lower sides of the circular cylinder. The straight (dashed) line denotes the positive (negative) values. After Inoue and Hatakeyama (2002).

Hatakeyama (2002) studied the effect of Mach number on the sound generated and the generation mechanism of the sound from flow over a circular cylinder by numerically solving the compressible Navier-Stokes equations using the finite difference method. It was found that the lift coefficient was not affected significantly when the Mach number was increased (The Mach number was varied from 0.1 to 0.3 in their study), whereas the mean value of the drag coefficient slightly increases as the Mach number is increased. The Strouhal number was observed to be constant for different Mach numbers. The sound pressure wave was observed to be generated mainly from the alternating shedding of vortices from the circular cylinder. When the vortex is shedding from the upper side of the circular cylinder, the negative and positive pressure pulses are generated from the upper and lower sides of the cylinder, respectively, as shown in Figure 1.1. On the other hand, when the vortex is shedding from the lower side of the

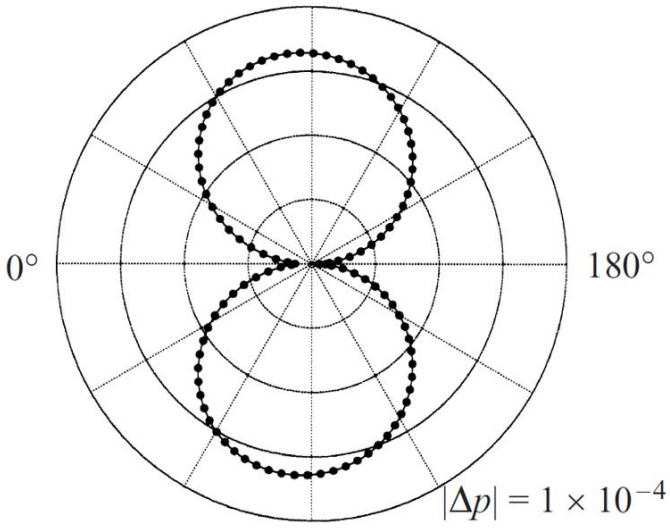

Figure 1.2 Polar plot of root mean square of the fluctuation pressure generated from flow past circular cylinder. M = 0.2, Re = 150. After Inoue and Hatakeyama (2002).

circular cylinder, the negative and positive pressure pulses are generated from the lower and upper sides of the cylinder, respectively. As the process goes on, the pressure wave is continuously generated from the cylinder. The analysis of the sound in the far field shows that sound is mostly generated by the lift dipole, the unsteady lift force, as shown in Figure 1.2. Only a small amount of sound was generated by the fluctuation of the drag force or quadrupole source. The propagation angle of sound wave that is bent from a right angle to the inflow direction is a result of the Doppler effect and it is bent more in the upstream direction with increasing Mach number. The sound pressure wave was well predicted by the Curle's solution when the mean pressure was removed from the solution and was observed to decay as it propagated away from the cylinder following the inverse square law in agreement with the Curle's analogy.

The sound generated by flow past a rectangular cylinder and multi-rectangular cylinders has also been studied both experimentally and computationally (Liow et al., 2006; Inoue, Mori, and Hatakeyama, 2006; Inoue, Iwakami, and Hatakeyama, 2006; Inasawa et al., 2013). The sound generated by flow past a rectangular cylinder had been studied by Inasawa et al. (2013) by directly solving the compressible Navier-Stokes equations using the finite difference method at low Mach numbers and low Reynolds numbers. They found that the frequency of vortex shedding was affected by the aspect ratio of the rectangular cylinder, thus leading to the different

sound generated. It is normal that changing the geometry or the configuration of the bluff body such as changing the aspect ratio of the rectangular cylinder (Inasawa et al., 2013), varying the space between two cylinders (Inoue, Mori, and Hatakeyama, 2006; Inoue, Iwakami, and Hatakeyama, 2006), adding a flat plate next to the bluff body (Ali, Doolan, and Wheatley, 2011), or varying the incident angle (Sandberg et al., 2009; Margnat, 2015) will result in the different sound generated because that is likely to alter the flow parameters, thus leading to the different sound emitted. Apart from the predominant sound generated by vortex shedding and varied for the different geometry of the cylinder, the frequency that is not associated with the vortex shedding might also be observed such as the frequency associated with the secondary vortex street developed behind the rectangular cylinder at low Mach and Reynolds numbers (Inasawa et al., 2013).

As for the equilateral triangular cylinder, one of the basic geometries in my opinion, seem to have received far less attention. Bao, Zhou, and Zhao (2010), Tu et al. (2014), and Ng et al. (2016) numerically studied the incompressible flow past a triangular cylinder and found that the flow parameters such as the mean value of the drag coefficient, the root mean square of the lift coefficient, and the Strouhal number were significantly affected by the attack angle between the flow and the triangular cylinder. Changing the incident angle and the Reynolds number would result in the shift of the separation point, thus, leading to the change in the flow field. Ng et al. (2016) reported that five different types of vortex streets occurred in unsteady flows past a triangular cylinder between the Reynolds numbers 80 and 200. The observed vortex streets are, as shown in Figure 1.3, the Bénard-von Kármán vortex street, the bi-layered wake arrangement, the secondary vortex street, the *P+S*-like wake, and the *2P*-like wake. The Bénard-von Kármán vortex street, as described by Ng et al. (2016), is a wake of the vortices in which one single sign of a vortex are shed alternately and was observed at a low Reynolds number for any incident angle. The wake is called the bi-layered wake arrangement if the vortices advected downstream reform into two simple shear layers with a different sign. If the vortices then rearrange itself into another vortex street of a larger scale, it is called the secondary vortex street. If in one shedding cycle a pair of vortices with opposite sign and a single vortex are alternately shedding from the

cylinder, it is called the *P+S*-like wake. Lastly, it is called the *2P*-like wake if two pairs of vortices with opposite sign are shed from each side of the cylinder.

Though the study of flow past the triangular cylinder has caught some researcher's attention, few of them focused on the study of the sound induced by the flow past the triangular cylinder. Ali et al. (2013) predicted an Aeolian tone radiated from flow over different shapes of bluff bodies (triangle, ellipse, circular, and square) by using the Curle's analogy at Reynolds number 150 and Mach number 0.2. They found that the fluctuation of the lift force acting on the triangular cylinder was highest among the other bluff bodies as shown in Table 1.1. Thus, by using the Curle's analogy, the sound generated by the triangular cylinder is the loudest among the other bluff bodies. The Stouhal number of the triangular cylinder was found to be the second highest also due to the shorter vortex formation. However, the sound generated from the triangular cylinder was studied at only one incident angle, that is when one of its vertices points in the direction of the incoming flow. Additionally, by using the Curle's analogy, the effect of mean pressure has been neglected from the calculated fluctuation pressure. Moreover, the authors used only the fluctuating lift force as a source term in the Curle's solution and had neglected the fluctuating drag force. Even though the fluctuating drag force is relatively small compared to that of the lift force, and so, contributes a smaller part to the overall sound, the fluctuation of the drag force was observed to increase as the Reynolds number is increased when the Reynolds number was low (Ng et al., 2016) and may be more important when predicting the sound generated by flow past a triangular cylinder at low Reynolds numbers.

Table 1.1 Stouhal number, root mean square of lift coefficient, mean value of drag coefficient, and root mean square of fluctuation pressure from flow over bluff bodies. After Ali et al (2013).

Bluff body	St	$C_{L,\mathrm{rms}}$	$C_{D,\mathrm{mean}}$	$\tilde{P}_{\mathrm{rms,80D}}$
Triangle	0.2143	0.4447	1.883	41.90 dB
Ellipse	0.2180	0.3927	1.474	40.77 dB
Circular	0.1880	0.3825	1.368	40.03 dB
Square	0.1600	0.2850	1.470	36.71 dB

1.2 Objectives

The purpose of this study is to study the characteristics of the aeroacoustic sound generated by flow past a triangular cylinder at different incident angles for selected Reynolds numbers 140, 160, and 180 at Mach number 0.3 by directly solving the compressible Navier Stokes equations using the OpenFOAM software. The Reynolds numbers was chosen to be 140, 160, and 180 so the obtained results could be compared with those from Tu et al. (2014) in which the Reynolds number was varied from 50 to 160, and those from Bao, Zhou, and Zhao (2010) in which the Reynolds number was varied between 100 and 150, and the results from Ng et al. (2016) in which the Reynolds number was varied from 80 to 200. The aeroacoustic forces, lift and drag will also be examined as the incident angle and the Reynolds number are varied and compared with the results reported by Bao, Zhou, and Zhao (2010), Tu et al. (2014), and Ng et al. (2016) for incompressible flows. The wake pattern developed behind the triangular cylinder will be observed and compared with the result reported by Ng et al. (2016) for incompressible flows.

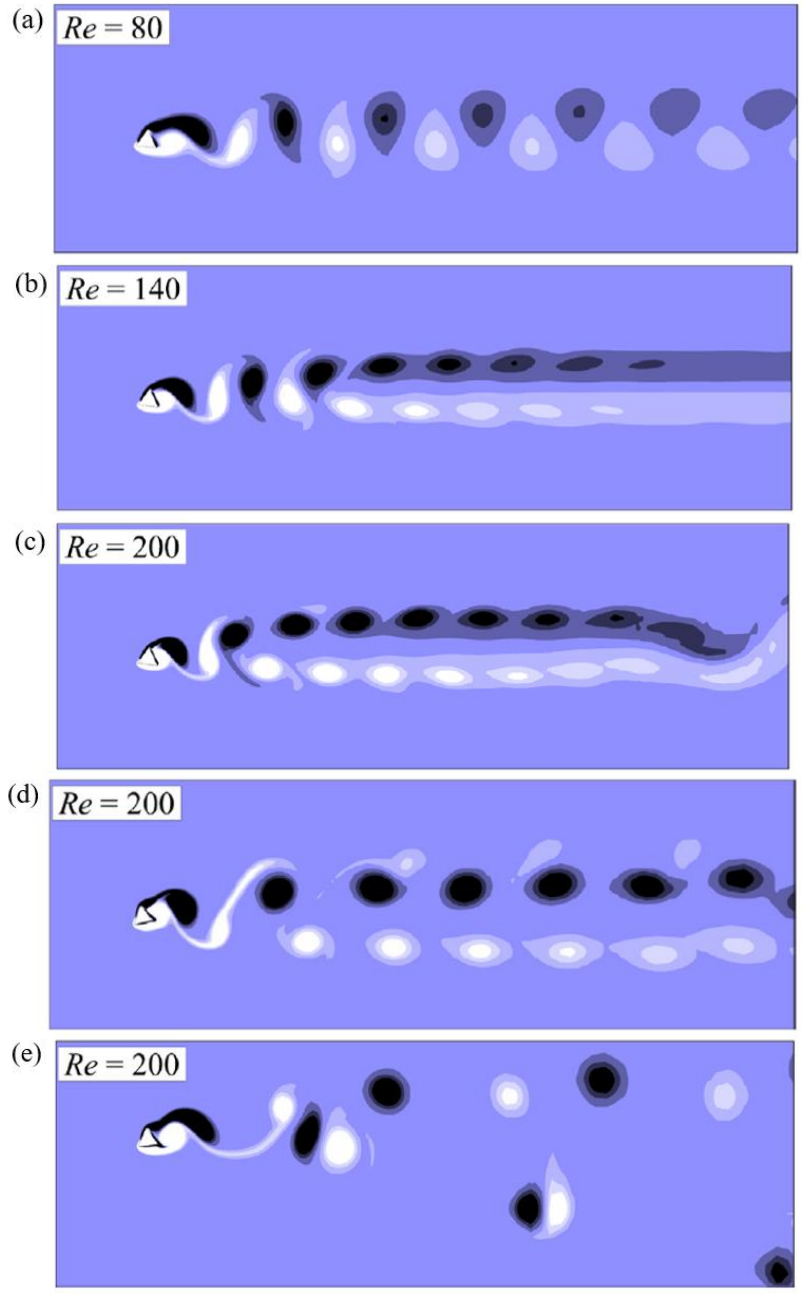

Figure 1.3 Vorticity fields of the wakes developed by flow past triangular cylinder. (a) The Bénard-von Kármán vortex street. (b) The bi-layered wake arrangement. (c) The secondary vortex street. (d) The *P*+*S*-like wake. (e) The *2P*-like wake. After Ng et al. (2016).

CHAPTER II
THEORY

In this chapter, theories related to this study will be given. In the first section, the Navier-Stokes equations governing the motion of compressible fluids will be given along with some concepts of thermodynamics. In the second section, the dimensionless numbers employed in this study will be briefly explained. In the last section, the basic of aeroacoustics will be briefly described and we mainly focus on Lighthill's equation and Curle's analogy.

2.1 The equation of fluid motion

In this section, the equations related to the conservation of mass, momentum, and energy will be given. Some concepts of thermodynamics will also be described.

2.1.1 Continuity equation

The continuity equation is the differential equation deduced from the conversation of mass. It states that the mass is neither created nor destroyed in any fluid element. The continuity equation with no source or sink terms is written, in index notation, as

$$\frac{\partial \rho}{\partial t} + \frac{\partial}{\partial x_i}(\rho u_i) = 0 \tag{2.1}$$

with ρ being the fluid density, and u_i the fluid velocity in the x_i-direction. For incompressible flows when the density is constant, the continuity equation reduces to

$$\frac{\partial u_i}{\partial x_i} = 0. \tag{2.2}$$

2.1.2 The momentum equation

The momentum equation, as its name suggests, is a statement of conservation of momentum in fluid and is derived from the Newton's second law of motion. It relates the fluid acceleration to the net body and surface forces exerting on the fluid. The momentum equation is written as

$$\frac{\partial}{\partial t}(\rho u_j) + \frac{\partial}{\partial x_i}(\rho u_i u_j) = \rho g_j + \frac{\partial}{\partial x_i}(T_{ij}), \tag{2.3}$$

where T_{ij} is the stress tensor, and g_j the body force in the x_j-direction. The stress tensor T_{ij} represents the surface force acting on the fluid element. The first index of T_{ij} indicates the direction of the surface normal at which the stress acts, and the second index indicates the direction of the stress acting. The diagonal elements of T_{ij} represent the normal stresses, while the off-diagonal elements represent the shear stresses. For a moving fluid, the stress tensor is

$$T_{ij} = -p\delta_{ij} + \tau_{ij}, \tag{2.4}$$

where p is the thermodynamic pressure, and τ_{ij} the viscous stress tensor. It can be shown that for an incompressible flow the stress tensor T_{ij} is in the form

$$T_{ij} = -p\delta_{ij} + 2\mu S_{ij}, \tag{2.5}$$

where

$$S_{ij} = \frac{1}{2}\left(\frac{\partial u_i}{\partial x_j} + \frac{\partial u_j}{\partial x_i}\right) \tag{2.6}$$

is the strain rate tensor and depends on the velocity gradient, and μ the dynamic viscosity. For the stress tensor of a compressible flow, the second viscosity coefficient or the coefficient of bulk viscosity μ_v is needed and was shown to be

$$T_{ij} = -p\delta_{ij} + 2\mu\left(S_{ij} - \frac{1}{3}S_{mm}\delta_{ij}\right) + \mu_v S_{mm}\delta_{ij}, \tag{2.7}$$

where the term $S_{mm}\delta_{ij} = \nabla \cdot \mathbf{u}$ is the divergence of velocity. This second viscosity coefficient is related to the rate of expansion of fluid and sometimes can be neglected, called the Stokes hypothesis. The Stokes hypothesis can be used to further simplify the stress tensor by assuming the bulk viscosity to be zero expressing that the change of volume does not involve viscosity. A fluid whose stress tensor satisfies Equation (2.7) is referred to as a Newtonian fluid.

2.1.3 The energy equation

The energy equation can be written in many different ways, the one below is given in the form that the specific total energy is a dependent variable. The energy equation is derived from the first law of thermodynamics and given by

$$\frac{\partial}{\partial t}\left(\rho\left[e+\frac{1}{2}u_j^2\right]\right)+\frac{\partial}{\partial x_i}\left(\rho\left[e+\frac{1}{2}u_j^2\right]u_i\right)=\rho g_i u_i+\frac{\partial}{\partial x_i}\left(T_{ij}u_j\right)-\frac{\partial q_i}{\partial x_i}, \quad (2.8)$$

where the term in the square bracket is the total energy per unit mass of the fluid equal to the sum of its specific internal energy e and its kinetic energy per unit mass $\frac{1}{2}u_i^2$, and q_i the heat flux in the x_i-direction. The energy equation describes the relation among the rate of change of the total energy, the work done by the body force g_i, the work done by the stresses T_{ij}, and the heat transfer process. The heat flux q_i is a vector field describing the heat conduction due to the temperature gradient in the flow field and related to the temperature by the Fourier's law given by

$$q_i=-k\frac{\partial T}{\partial x_i}, \quad (2.9)$$

where k is the heat conductivity coefficient. For incompressible flows the density is constant, so it can be taken out of the derivatives. If the viscosity μ is constant, then the energy equation can be decoupled from the continuity and momentum equations. Commonly, solving the energy equation is not a primary concern in an incompressible flow and only will be solved if the heat transfer process is involved in the system of interest.

2.1.4 Thermodynamics quantities

In this subsection, we review some concepts of thermodynamics. The first law of thermodynamics states that the energy of a system is conserved,

$$\Delta e=\delta q+\delta w, \quad (2.10)$$

where Δe is the change of internal energy per unit mass of the system, δq the heat added per unit mass, and δw the work done on the system per unit mass. For a compressible fluid, the work done δw is by the expansion or contraction except the work by the irreversible form of works such as from the friction force. The first law of thermodynamics becomes

$$de=\delta q-pdv, \quad (2.11)$$

where dv is a change in volume per unit mass related to the fluid density by $v = 1/\rho$. By defining a thermodynamics property called the specific enthalpy by

$$h \equiv e + pv, \tag{2.12}$$

we can show that

$$dh = \delta q + vdp = \delta q + \frac{1}{\rho}dp. \tag{2.13}$$

The specific heat capacities at constant pressure and constant volumes are defined as

$$c_p \equiv \left(\frac{\partial h}{\partial T}\right)_p = \left(\frac{\partial q}{\partial T}\right)_p, \tag{2.14}$$

$$c_v \equiv \left(\frac{\partial e}{\partial T}\right)_v = \left(\frac{\partial q}{\partial T}\right)_v, \tag{2.15}$$

respectively. In ideal gas, the internal energy e and enthalpy h are function of temperature only. Thus,

$$dh = c_p dT, \tag{2.16}$$

$$de = c_v dT. \tag{2.17}$$

For a calorically perfect gas, the specific heats are assumed to be constant so the internal energy and the enthalpy are related to the temperature by

$$h = c_p T, \tag{2.18}$$

$$e = c_v T. \tag{2.19}$$

The perfect gas law can be obtained from Equations (2.12), (2.18), and (2.19) as

$$p = \rho RT, \tag{2.20}$$

where $R = c_p - c_v$ is the specific gas constant. The second law of thermodynamics states that the entropy of an isolated system can never decrease over time

$$\Delta s \geq \int \frac{\delta q}{T}, \tag{2.21}$$

where the equal sign applies for the reversible process. For a reversible process, the entropy change equals the heat added divided by the temperature of the system. Hence,

$$de = Tds - pdv, \tag{2.22}$$

$$dh = Tds - vdp. \tag{2.23}$$

The change in specific entropy of perfect gas can be shown to be

$$ds = c_v \frac{dp}{p} - c_p \frac{d\rho}{\rho}. \tag{2.24}$$

We then have the relation for entropy by integrating Equation (2.24) to give

$$s = c_v \ln\left(\frac{Cp}{\rho^\gamma}\right), \tag{2.25}$$

where C is the constant of integration, and $\gamma = c_p/c_v$ the ratio of specific heats. If the flow is isentropic, that is, both adiabatic and reversible, the entropy of the system does not change during a process. Additionally, if the entropy is the same everywhere, the flow is said to be homentropic. If the entropy is constant, then

$$\frac{p}{\rho^\gamma} = \text{const.} \tag{2.26}$$

Upon differentiating Equation (2.26) with respect to ρ, we have a relation

$$\left(\frac{\partial p}{\partial \rho}\right)_s = \frac{\gamma p}{\rho}, \tag{2.27}$$

where γp is the isentropic bulk modulus K_s of the fluid. The idea of isentropic flow is applicable in a normal acoustic situation, by assuming that the process of propagating sound wave is very fast compared to the heat dissipation rate. The compression and rarefaction processes happen at a very fast rate compared to the heat exchange process. Hence, the process is assumed to be adiabatic because no heat is transferred during the process. Additionally, if the work only consists of reversible work (compression and rarefaction with irreversible works excluded), then the process is reversible and thus the process is isentropic. The square root of Equation (2.27) is the definition of speed of sound c

$$c = \sqrt{\left(\frac{\partial p}{\partial \rho}\right)_s}. \tag{2.28}$$

In incompressible fluids, the change in fluid density is zero so the speed of sound is infinite and the Mach number is zero. For a perfect gas, the speed of sound is

$$c = \sqrt{\frac{\gamma p}{\rho}} = \sqrt{\gamma RT}, \tag{2.29}$$

Since in a normal acoustic process, the fluctuations in pressure and density are very small compared to their mean value so their absolute values can be replaced by their mean values as

$$c_0 = \sqrt{\frac{\gamma p_0}{\rho_0}}, \tag{2.30}$$

By expanding the pressure about its reference value with the condition of isentropic flow, the fluctuation pressure and density can be related by

$$\begin{aligned} p &= p_0 + p' \\ &= p_0 + \left(\frac{\partial p}{\partial \rho}\right)_s (p - p_0) + \frac{1}{2}\left(\frac{\partial^2 p}{\partial \rho^2}\right)_s (p - p_0)^2 + \cdots \\ &= p_0 + c^2\rho' + \frac{1}{2}\left(\frac{\partial^2 p}{\partial \rho^2}\right)_s (p - p_0)^2 + \cdots \end{aligned} \tag{2.31}$$

Neglecting the second-order and higher-order terms gives the relation

$$p' = c^2\rho', \tag{2.32}$$

This relation is often used in acoustics for expressing the fluctuation density ρ' in terms of fluctuation pressure p'.

2.1.5 Equation of state

For compressible flows, the equation of states relating the state variables are needed to link the density, pressure, and temperature in order to close the system. In aeroacoustics, it is generally assumed that the gas is perfect gas. For a perfect gas, the thermal equation of state relating thermodynamic variables is

$$p = \rho RT, \tag{2.33}$$

where R is the specific gas constant. If more equations are needed to close the system, the caloric equations of state relating the internal energy and the temperature in Equations (2.18), (2.19) can be used.

2.2 Dimensionless numbers

In fluid mechanics, the dimensionless numbers are the numbers that are useful for predicting the flow characteristics of a fluid. It is typically defined as a ratio of quantities having units of identical dimension. In this section, we give the description of the dimensionless numbers related to this study, the Reynolds number, the Mach number, the Strouhal number, and the Prandtl number.

2.2.1 Reynolds number

The Reynolds number is defined as the ratio of fluid inertial forces to its viscous forces. At a low Reynolds number, the flow is dominated by the viscous forces and the flow is laminar. When the Reynolds number exceeds a certain threshold, a non-fully turbulent flow occurs. This regime is referred to as the transition regime. Over a certain range of value of the Reynolds number, the flow is dominated by the inertial forces and becomes fully turbulent. The Reynolds number is written as

$$\mathrm{Re} = \frac{\rho U d}{\mu} = \frac{U d}{\nu}, \tag{2.34}$$

where ρ is the fluid density, U the flow velocity, d the characteristic length, μ and ν the dynamic and kinematic viscosities, respectively. The threshold value of the Reynolds number where the flow transitions from laminar to turbulence is called the critical Reynolds number ($\mathrm{Re}_{\mathrm{cr}}$) and different for each flow situation. For flow around a sphere, the critical Reynolds number is approximately 2×10^5.

2.2.2 Mach number

The Mach number measures the compressibility of the fluid flow and is defined as the ratio of flow velocity to the speed of sound in the surrounding fluid given by

$$\mathrm{M} = \frac{U}{c}, \tag{2.35}$$

where c is the sound speed in the fluid. Flows in which the Mach number is smaller than unity anywhere in the flow field are called subsonic, whereas flows in which the Mach number is greater than unity are called supersonic. The flows are considered to be incompressible flow if the Mach number is less than 0.3 because of the negligible effect of the temperature on the density.

2.2.3 Strouhal number

The Strouhal number is a dimensionless number describing the oscillation mechanism of the flow. It is defined as the ratio of inertial forces due to the unsteadiness acceleration of the flow to the inertial forces due to the convective acceleration, given by

$$\mathrm{St} = \frac{fU}{D}, \tag{2.36}$$

where f is the frequency of vortex shedding. For a circular cylinder, the Strouhal number remains close to 0.2 and slightly varies for a large range of Reynolds number.

2.2.3 Prandtl number

The Prandtl number is a dimensionless number defined as the ratio of momentum diffusivity to thermal diffusivity, expressed by

$$\mathrm{Pr} = \frac{c_p \mu}{k}, \tag{2.37}$$

where c_p is the specific heat, and k the heat conductivity. For air, the Prandtl number is 0.71.

2.3 Aeroacoustics

Aeroacoustics is the field that studies the sound that is generated via the fluid motion. It was first originated in the early 1950s with the invention of the jet engine because the very loud sound radiated from the exhausted jet cannot be explained by the theory of linear acoustics. In 1952, the first paper explaining how the fluid motion generates sound was published by M. J. Lighthill. By rearranging the continuity equation and the momentum equation to the Lighthill's equation, an inhomogeneous wave equation, the acoustic sound source can be determined.

2.3.1 Sound

Sound is a mechanical wave produced by vibration and is transmitted through the medium. When the sound wave is travelling, it causes the medium to compress and expand alternately. Sound waves travel at different speeds on each medium, usually fastest in solid, slower in fluid, and slowest in air. The sound speed in air is approximated by

$$c_{\mathrm{air}} = (331.3 + 0.606T)\ \mathrm{m/s}, \tag{2.38}$$

where T is the temperature in degrees Celsius. Because human ears can detect a wide range of pressure fluctuation from a very small fluctuation like 20 μPa (0 dB) to a very

large fluctuation like 200 Pa (140 dB), a logarithmic scale is thus used to measure the intensity of the sound pressure humans experience in everyday life. Sound pressure level (SPL) is a logarithmic measure of the sound pressure with the common unit decibel defined as

$$L_p = 20\ \log_{10}\left(\frac{p_{\mathrm{rms}}}{p_{\mathrm{ref}}}\right)\ \mathrm{dB}, \tag{2.39}$$

where p_{rms} is the root mean square of the fluctuating pressure, and p_{ref} the reference sound pressure. In air, the reference sound pressure is 20 μPa. In a normal acoustic situation, i.e., small perturbations, isentropic, and stationary medium with no source term, the linear wave equation describing the propagation of acoustic waves is written as

$$\frac{1}{c^2}\frac{\partial^2 p'}{\partial t^2} - \frac{\partial^2 p'}{\partial x_i \partial x_i} = 0, \tag{2.40}$$

which is known as the classical wave equation. The one-dimensional solution to this wave equation is in the form

$$p'(x,t) = f(x-ct) + g(x+ct), \tag{2.41}$$

where the functions f and g are determined by the initial conditions. The functions $f(x-ct)$ and $g(x+ct)$ represent the waves propagating to the right and left, respectively, with a constant speed c.

2.3.2 Lighthill's equation and Curle's analogy

The Lighthill's equation describing the propagation of an acoustic wave in a stationary medium generated from a region of turbulent flow is written as

$$\frac{\partial^2}{\partial t^2}(\rho-\rho_0) - c_0^2\frac{\partial^2}{\partial x_i^2}(\rho-\rho_0) = \frac{\partial^2 T_{ij}}{\partial x_i \partial x_j}, \tag{2.42}$$

where

$$T_{ij} = \rho u_i u_j + (p-p_0)\delta_{ij} - (\rho-\rho_0)c_0^2\delta_{ij} - \tau_{ij} \tag{2.43}$$

is called Lighthill's stress tensor and is referred to as a source term, the subscript 0 is referred to the ambient value, and c_0 the sound speed in the medium at rest. Note that this Lighthill's stress tensor T_{ij} is different from the stress tensor in Section 2.1. The solution to the Lighthill's equation when the medium is unbounded is in the integral form of the retarded potential as

$$\rho(\mathbf{x},t)-\rho_0=\frac{1}{4\pi c_0^2}\frac{\partial^2}{\partial x_i\partial x_j}\int_V \frac{T_{ij}(\mathbf{y},t')}{r}dV(\mathbf{y}), \tag{2.44}$$

where $t'=t-r/c_0$ is the retarded time, and $r=|\mathbf{x}-\mathbf{y}|$ with **x** and **y** refer to observer and source coordinates, respectively. Generally in flow at a high Reynolds number and a low Mach number, the Lighthill's stress tensor can be approximated by $T_{ij}\approx\rho_0 u_i u_j$ since the contribution from the other terms is small. In the presence of solid boundaries, the general solution of Lighthill's equation can be shown, using the method of Green's function, to be

$$\begin{aligned}\rho(\mathbf{x},t)-\rho_0=&\frac{1}{4\pi c_0^2}\frac{\partial^2}{\partial x_i\partial x_j}\int_V \left[T_{ij}\right]_{t'}\frac{dV(\mathbf{y})}{r}\\&-\frac{1}{4\pi c_0^2}\frac{\partial}{\partial x_i}\int_S \left[p_{ij}+\rho u_i u_j\right]_{t'}\frac{n_j dS(\mathbf{y})}{r}\\&+\frac{1}{4\pi c_0^2}\int_S \left[\frac{\partial(\rho u_j)}{\partial t}\right]_{t'}\frac{n_j dS(\mathbf{y})}{r}\end{aligned} \tag{2.45}$$

where $p_{ij}=(p-p_0)\delta_{ij}-\tau_{ij}$ is compressive stress tensor, and n_j the unit vector normal to surface S. Note that the source terms in square brackets are evaluated at the retarded time $t'=t-r/c_0$. If the surface is fixed or is vibrating in the surface plane, then $u_j n_j=0$ and Equation 2.16 reduces to

$$\begin{aligned}\rho(\mathbf{x},t)-\rho_0=&\frac{1}{4\pi c_0^2}\frac{\partial^2}{\partial x_i\partial x_j}\int_V \left[T_{ij}\right]_{t'}\frac{dV(\mathbf{y})}{r}\\&-\frac{1}{4\pi c_0^2}\frac{\partial}{\partial x_i}\int_S \left[P_i\right]_{t'}\frac{dS(\mathbf{y})}{r},\end{aligned} \tag{2.46}$$

where

$$P_i=p_{ij}n_j, \tag{2.47}$$

is the force per unit area exerting on the fluid by the solid boundaries in the x_i-direction. Equation (2.45) is often referred to as the Curle's analogy and it represents the sound generated by each source. The volume integral represents the sound generated from the turbulent motion of the flow and is associated with the quadrupole source, whereas the surface integral represents the sound generated by the force exerting on the boundary and is associated with the dipole source. Assuming that the flow contains no change in entropy, i.e., the flow is isentropic, the density fluctuation can be related to the pressure fluctuation using Equation (2.32). The Curle's analogy then becomes

$$p(\mathbf{x},t)-p_0=\frac{1}{4\pi}\frac{\partial^2}{\partial x_i\partial x_j}\int_V \left[T_{ij}\right]_{t'}\frac{dV(\mathbf{y})}{r}-\frac{1}{4\pi}\frac{\partial}{\partial x_i}\int_S \left[P_i\right]_{t'}\frac{dS(\mathbf{y})}{r}. \quad (2.48)$$

By using the dimensional analysis, assuming that the source is acoustically compact and the flow is isentropic, the fluctuation pressure is estimated to be proportional to the Mach number by the relation

$$p-p_0\propto\left(AM^{7/2}+M^{5/2}\right)/r^{1/2}, \quad (2.49)$$

where A is constant. Thus, in flow at sufficiently low Mach numbers, the first term can be neglected and the sound field is dominated by the second term, i.e., by the fluctuating force exerted on the boundaries.

CHAPTER III
NUMERICAL METHODS

In this chapter, the numerical method and the calculation details will be given. The geometry of the cylinder in the square domain and its mesh both were created in Gmsh software. Then, the mesh was imported to OpenFOAM to be numerically solved. In the final process, the vorticity field obtained from OpenFOAM was visualized in ParaView. The lift and drag coefficients and the pressure field are plotted and calculated for their mean values, root mean squared values, and spectra in MATLAB.

3.1 Geometry model

The geometry model of this study is depicted in Figure 3.1. The triangular cylinder with side length d is located at the middle of the square domain of size $620d$. The fluid with velocity U_∞ flows from the left to the right sides of the domain. The incident angle α is 0° when the vertex of the triangular cylinder points straight in the upstream direction. The incident angle α increases when the cylinder is rotated counterclockwise and ends up at $\alpha = 60°$ because of the symmetry of the cylinder. In the study, α starts from 0° to 60° in increment of 6°. The Reynolds number in this study is defined as

$$\mathrm{Re} = \frac{U_\infty h}{\nu}, \tag{3.1}$$

where h is called the frontal height (Ng, 2016) and is related to the cylinder side length d by the relation

$$\frac{h}{d} = \sin(60° - |\alpha - 30°|) + \sin(|\alpha - 30°|). \tag{3.2}$$

The values of the Reynolds number in this study are Re = 140, 160, and 180 so that the results can be compared to the results from Ng et al. (2016) for incompressible flow. The Mach number in this study is defined as

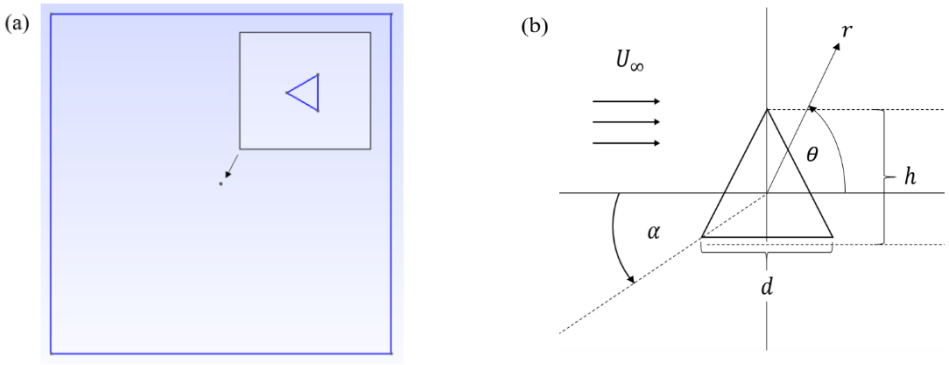

Figure 3.1 The triangular cylinder is at the middle of the rectangular domain. (b) The incident angle α is 0° when its vertex points in the upstream direction and increases when the cylinder is rotated counterclockwise.

$$\mathrm{M} = \frac{U_\infty}{c_0}, \tag{3.3}$$

where c_0 is the speed of sound in the rest fluid, and is set to be 0.3 throughout the study.

3.2 Preprocessing

Firstly, the triangular cylinder in the square domain was created in Gmsh software, a free mesh generator with a built-in CAD. The side length of the cylinder and the square domain was first built to be 2 m and 1240 × 1240 m^2 (will be scaled later in OpenFOAM) respectively. The triangular mesh was generated also in Gmsh and exported with the extension .geo. Figure 3.2 shows the triangular mesh near the cylinder. Secondly, the mesh file was then imported to OpenFOAM to solve for a numerical solution (will be given in the next section). In OpenFOAM, the geometry was scaled by 0.01 in both x and y directions. Hence, the side length of the cylinder and the size of the domain become 0.02 m and 12.4 12.4 m^2, respectively.

Because the default setting of the selected solver in OpenFOAM is not a dimensionless solver, the parameters had to be chosen to satisfy the required Reynolds number. One example is, for the selected fluid in this study, air, at Re = 160 and $\alpha = 36°$. The dynamic viscosity μ is set to 0.01416 kg/(m·s), thus

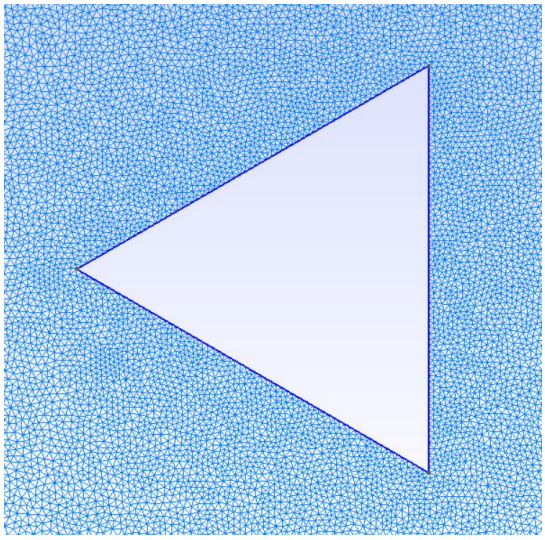

Figure 3.2 The zoomed image of the region near the triangular cylinder for $\alpha = 0°$ shows the triangular mesh by Gmsh.

$$\text{Re} = \frac{\rho_\infty U_\infty h}{\mu} = \frac{(1.202)(103.14)(0.01827)}{0.01416} \approx 160.$$

All values of dynamics viscosity for different Reynolds numbers and incident angles are given in Appendix A. By choosing the working fluid as air, the velocity inlet U_∞ was set to be 103.14 m/s to give the resultant Mach number

$$M = \frac{U_\infty}{c_0} = \frac{103.14}{343.8} \approx 0.3.$$

In this study, the viscosity and the thermal conductivity are taken to be constant during each simulation because the temperature does not significantly affect the transport properties at low Mach numbers (Inoue, 2006). The Prandtl number Pr was set to be 0.713.

To test that changing μ for each α and Re will not affect the numerical solution significantly, the preliminary experiment has been done by comparing three cases of flow past the triangular cylinder at the same $\alpha = 0°$ and Re = 150. One is by setting $d = 0.002$ m and $\mu = 1.6523 \times 10^{-3}$ kg/(m·s), the second is $d = 0.02$ m and $\mu = 1.6523 \times 10^{-2}$ kg/(m·s), and the third is $d = 0.2$ m and $\mu = 1.6523 \times 10^{-1}$ kg/(m·s). The results, presented in Figure 3.3, show that the lift and drag coefficients, and the pressure at three locations obtained from the simulations when plotted against non-dimensional time tU_∞/d are the same, i.e., the results from the three cases

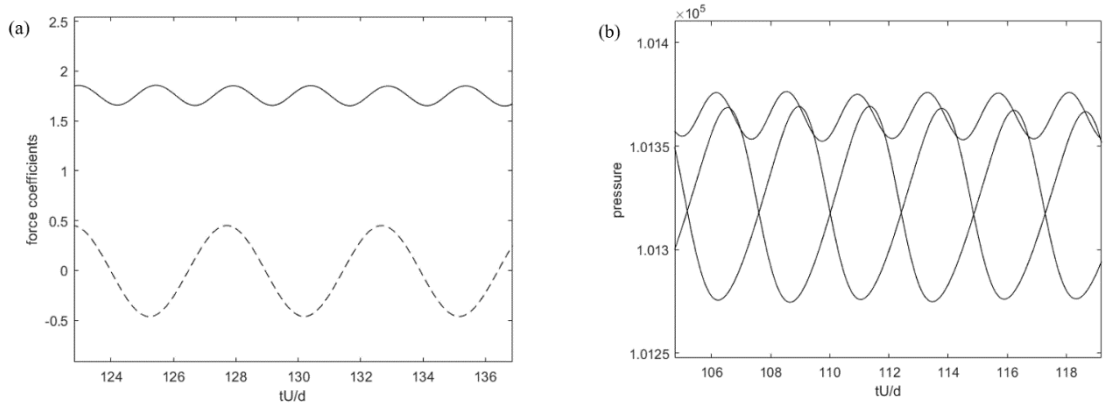

Figure 3.3 The time histories of (a) lift and drag coefficients and (b) pressure at three locations for three cases of flow past triangular cylinder at $\alpha = 0°$ and Re = 150.

completely overlap each other. Therefore, we can vary the dynamics viscosity μ for each α and Re.

Probing

The probe function in OpenFOAM was used for collecting the pressure data over time at the desired locations. There are three types of probe employed in this study. In Type I, the probes are located at three points, using the polar coordinates, $(r, \theta) = (75d, \pm 90°)$ and $(75d, 180°)$. This type is used for comparing the similarity and difference of the sound pressure wave received at the three points. Type II is used for investigating the decay of the pressure wave as the wave propagates away from the cylinder and located from $(r, \theta) = (10d, \pm 90°)$ to $(100d, \pm 90°)$ having 46 probes for each side. Type III is used in studying the directivity of the pressure wave generated and located around the cylinder, that is $(r, \theta) = (75d, 0°)$ to $(75d, 360°)$ consisting of 80 probes uniformly spaced.

3.3 Numerical Method for solving the governing equations

3.3.1 Overview of OpenFOAM

OpenFOAM stands for Open-Source Field Operation And Manipulation is open-source software popularly used for computational fluid dynamics (CFD) applications. OpenFOAM has been continuously updated and the latest version is

OpenFOAM 8 and was released on July 2020. Basically, OpenFOAM uses the finite volume method to solve a set of governing equations which is determined by the solver selected. The solver which the user has to choose will determine the governing equations and the algorithm used in solving the equations. The examples of available solvers are `icoFoam' which solves for incompressible, laminar flows of Newtonian fluids, `simpleFoam' solves for steady state of incompressible, turbulent flows by using the SIMPLE algorithm, `interFoam' solves two incompressible, isothermal immiscible fluids, `rhoSimpleFoam' solves for steady state solution of turbulent, compressible flows. Other than applications in CFD, there available solvers for electromagnetic, financial, applications.

3.3.2 Finite volume method

The finite volume method (FVM) is a discretization method for the partial differential equations. In the finite volume method, the computational domain to be numerically solved for the solution of such partial differential equation is subdivided into smaller elements called control volumes or finite volumes. We first consider the general transport equation in the form

$$\frac{\partial}{\partial t}(\rho\phi) + \nabla \cdot (\rho \mathbf{u}\phi) - \nabla \cdot \left(\rho \Gamma^{\phi} \nabla \phi \right) = Q^{\phi}, \tag{3.4}$$

with ϕ being the quantity to be transported, the terms on the left-hand side are the local rate of change, the rate of the change due to the convection, and the diffusion term, respectively. The one on the right-hand side is referred to as a source term, and Γ^{ϕ} is the diffusion coefficient of ϕ. Integrating both sides of the equation over the control volume yields

$$\int_{V_c} \frac{\partial}{\partial t}(\rho\phi)\, dV + \int_{V_c} \nabla \cdot (\rho \mathbf{u}\phi)\, dV - \int_{V_c} \nabla \cdot \left(\rho \Gamma^{\phi} \nabla \phi \right) dV = \int_{V_c} Q^{\phi}\, dV. \tag{3.5}$$

The second and the third terms on the left-hand side can be converted to surface integrals using the Gauss' theorem stating that the volume integral of divergence of a vector field **F** equals the surface integral of its flux bounded by that volume, or

$$\int_{V} (\nabla \cdot \mathbf{F})\, dV = \int_{\partial V} \mathbf{F} \cdot d\mathbf{S}. \tag{3.6}$$

Equation (3.5) then becomes

$$\int_{V_c} \frac{\partial}{\partial t}(\rho\phi)\, dV + \int_{\partial V_C} (\rho \mathbf{u}\phi) \cdot d\mathbf{S} - \int_{\partial V_C} \left(\rho \Gamma^{\phi} \nabla \phi \right) \cdot d\mathbf{S} = \int_{V_c} Q^{\phi}\, dV\,. \quad (3.7)$$

Denoting the convective flux $\rho \mathbf{u}\phi$ and diffusive flux $-\rho\Gamma^{\phi}\nabla\phi$ by $\mathbf{J}^{\phi,C}$ and $\mathbf{J}^{\phi,D}$, respectively. To calculate the fluxes convecting across the surface of the control volume, the surface integrals in Equation (3.7) becomes

$$\int_{\partial V_C} \mathbf{J}^{\phi} \cdot d\mathbf{S} = \sum_{faces} \left(\int_f \mathbf{J}_f^{\phi} \cdot d\mathbf{S} \right), \quad (3.8)$$

with $\mathbf{J}^{\phi} = \mathbf{J}^{\phi,C} + \mathbf{J}^{\phi,D}$, and the integral is evaluated at all the faces of the control volume. The choice of surface integration is customary depending on the required accuracy. Typically, the midpoint rule where one integration point used for integration is employed. Equation (3.8) then becomes

$$\int_{\partial V_C} \mathbf{J}^{\phi} \cdot d\mathbf{S} = \sum_{faces} \mathbf{J}_f^{\phi} \cdot \mathbf{n}_f \Delta S_f, \quad (3.9)$$

with $\mathbf{J}_f^{\phi}$ being the value of $\mathbf{J}^{\phi}$ at the center of the face f. For the source term, the integration point is the same depending on the required accuracy. If one-point integration is chosen, then

$$\int_{V_C} Q^{\phi} dV \approx Q_C^{\phi} V_C, \quad (3.10)$$

where V_C is the volume of the control volume, and Q_C^{ϕ} the value of Q^{ϕ} at cell centroid. The integral of the first term on the left-hand side of Equation (3.7) is simply

$$\int_{V_c} \frac{\partial}{\partial t}(\rho\phi)\, dV \approx \frac{\partial}{\partial t}(\rho\phi)_C V_C. \quad (3.11)$$

Equation (3.4) is finally in the form

$$\frac{\partial}{\partial t}(\rho\phi)_C V_C + \sum_{faces} \mathbf{J}_f^{\phi} \cdot \mathbf{n}_f \Delta S_f = Q_C^{\phi} V_C \quad (3.12)$$

The scheme for temporal discretization such as forward Euler, backward Euler, Crank-Nicolson, or Adam-Moulton methods are then selected to discretize the time derivative term depending on the required accuracy. In this work, the time discretization scheme

chosen is the forward Euler method. Hence, the time derivative term in Equation (3.12) is approximated by

$$\frac{\partial}{\partial t}(\rho\phi)_C V_C \approx \frac{(\rho\phi)_C^{t+\Delta t} - (\rho\phi)_C^t}{\Delta t} V_C \tag{3.13}$$

with the flux and the source terms being evaluated at time t. Thus, the value of $(\rho\phi)_C$ at time $t + \Delta t$ can be computed explicitly without solving a system of equations because all spatial terms are all known at the previous time step t as

$$(\rho\phi)_C^{t+\Delta t} = (\rho\phi)_C^t - \Delta t \left(\frac{1}{V_C} \sum_{faces} \mathbf{J}_f^\phi \cdot \mathbf{n}_f \Delta S_f - Q_C^\phi V_C \right) \tag{3.14}$$

3.3.3 Governing equations

After the mesh file is imported to OpenFOAM, the governing equations will be numerically solved by the selected solver using the finite volume method. In OpenFOAM, there are many solvers the user can choose to use, for instance, solver for incompressible or compressible flows, laminar or turbulence flows. For this study, the solver `rhoPimpleFoam' was selected. The rhoPimpleFoam solver, described in the manual as the transient solver for turbulent flow of compressible fluids for HVAC and similar applications, is employed. The rhoPimpleFoam solves the Navier-Stokes equations in the form

$$\frac{\partial \rho}{\partial t} + \nabla \cdot (\rho \mathbf{u}) = 0, \tag{3.15}$$

$$\rho \left(\frac{\partial \mathbf{u}}{\partial t} + \mathbf{u} \cdot \nabla \mathbf{u} \right) = -\nabla p - \nabla \cdot \tau, \tag{3.16}$$

$$\frac{\partial (\rho E)}{\partial t} + \nabla \cdot (\rho \mathbf{u} E) = -\nabla \cdot (p\mathbf{u}) + \nabla \cdot (\tau \cdot \mathbf{u}) - \nabla \cdot \mathbf{q} \tag{3.17}$$

where ρ is the fluid density, u the velocity, p the absolute pressure, τ the viscous stress tensor, E the total energy, and $\mathbf{q}$ the heat flux. For the air which is a Newtonian fluid, the Newton's law of viscosity states that the viscous stress is related to the velocity gradient by

$$\tau_{ij} = \mu \left(\frac{\partial u_i}{\partial x_j} + \frac{\partial u_j}{\partial x_i} \right) - \frac{2}{3} \mu \frac{\partial u_i}{\partial x_j} \delta_{ij} \tag{3.18}$$

Table 3.1 Types of boundary conditions applied at each boundaries.

	Variables			
	u_x	u_y	p	T
Inlet	$u_x = U_\infty$	$u_y = 0$	$\frac{\partial p}{\partial x} = 0$	$T = T_\infty$
Outlet	$\frac{\partial u_x}{\partial x} = 0$	$\frac{\partial u_y}{\partial x} = 0$	$\frac{Dp}{Dx} = 0$	$\frac{\partial T}{\partial x} = 0$
Cylinder surface	$u_x = 0$	$u_y = 0$	$\frac{\partial p}{\partial n} = 0$	$\frac{\partial T}{\partial n} = 0$

where μ is the dynamic viscosity of the fluid. The heat flux $\mathbf{q}$ in the energy equation is given by the Fourier's law of heat conduction indicating that the heat flow from high temperature region to a low temperature region

$$\mathbf{q} = -k\nabla T \tag{3.19}$$

with k being the thermal conductivity, and T the temperature. The equation of state is needed to close the system of equations. In this study, the system is at STP (standard temperature and pressure) and does not experience any extreme situation. Therefore, the ideal gas equation is suitable here,

$$p = \rho R_{\text{specific}} T \tag{3.20}$$

where $R_{\text{specific}} = 287.058$ J/kg·K is the specific gas constant of the air.

3.3.4 Boundary conditions and initial condition

Table 3.1 shows the boundary conditions used in this study. At the left boundary, the inlet boundary condition was applied. At the right boundary, the transmissive boundary condition in OpenFOAM was prescribed to prevent the wave reflecting back to the domain. On the cylinder surface, the adiabatic no-slip boundary condition was applied. The boundary conditions at the top and bottom boundaries were first set to be slip boundary condition but the simulation gave the same result as setting them to be inlet, so the inlet boundary condition was also applied at the top and bottom boundaries. The uniform flow was applied as the initial condition of the simulation, that is $u_x = U_\infty = 103.14$ m/s, and $u_y = 0$ m/s for the velocity. For pressure and temperature, $p = p_\infty = 101325$ Pa and $T = T_\infty = 293.15$ K, respectively.

3.4 Postprocessing

When the simulation finishes running, the outputs consist of the pressure field, velocity field, temperature field, vorticity field, the lift and drag coefficients, and the pressure at the probes' location. The lift and drag coefficients were calculated during the simulation by the formulas

$$C_L = \frac{2F_L}{\rho_\infty U_\infty^2 A_{\text{ref}}},$$

$$C_D = \frac{2F_D}{\rho_\infty U_\infty^2 A_{\text{ref}}},$$

where F_L is the lift force, F_D the drag force, ρ_∞ the reference density equal to 1.205 kg/m^3 for the air, and A_{ref} the reference area equal to 0.0002 m^2. The mean value (time-averaged) of a quantity was calculated as

$$A_{,\text{mean}} = \frac{1}{N}\sum_{i=1}^{N} A_i.$$

The root mean square of a quantity in this work was calculated about its mean average so

$$A_{,\text{rms}} = \sqrt{\frac{1}{N}\sum_{i=1}^{N} |A_i - A_{,\text{mean}}|^2}.$$

To calculate the power spectral density (PSD), the fft function in MATLAB is first operated on the time series data, then square its absolute value. The function fft computes the discrete Fourier transform of a signal using a fast Fourier transform (FFT) algorithm. In order to calculate the Stouhal number St, the Fourier transform was first operated to the lift coefficient C_L. The frequency with the highest magnitude f_{max} was used to calculate the Strouhal number, that is

$$\text{St} = \frac{f_{\text{max}} d}{U_\infty}.$$

The term fluctuation pressure is defined as

$$\Delta\tilde{p}(x, y, t) = p(x, y, t) - p_{\text{mean}}(x, y),$$

which is absolute pressure subtracted by its mean value. Figure~\ref{fig:output} shows the output data of lift and drag coefficients. In order to calculate the mean value, root mean square value, and spectral density of the lift coefficient, the drag coefficient, and

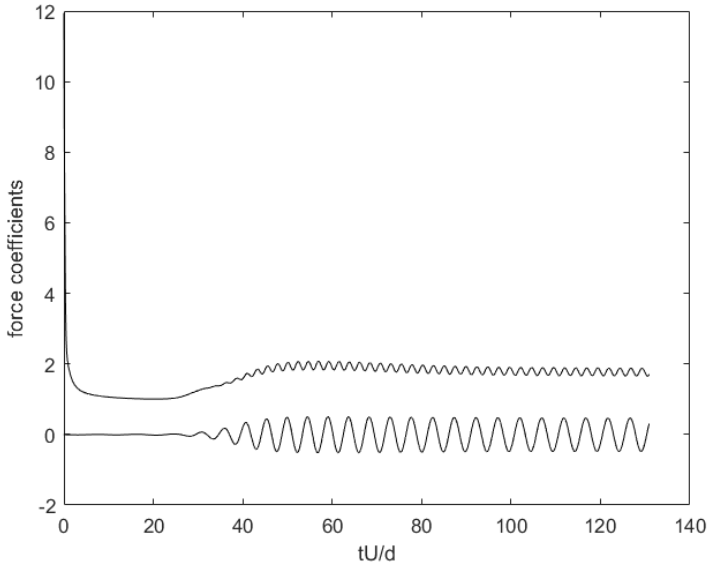

Figure 3.4 The time history of force coefficients obtained from the simulation.

the pressure, the interval of the data when the system reaches the steady state were selected to calculate the mean value, root mean square value, and spectral density (typically more than 10 wavelengths). To visualize the vorticity field, ParaView was employed.

CHAPTER IV
NUMERICAL RESULTS AND DISCUSSION

In this chapter, the numerical results obtained from the simulation and calculation will be given with the discussion. The lift and drag coefficients are examined explicitly with implication on the sound generated. The explanation of the generated sound associated with fluctuation of lift and drag coefficients will be given. The plots of directivity show that when the cylinder is symmetric, that is when $\alpha = 0°$ and 60°, the acoustic field is dominated by the lift dipole. When the cylinder is not symmetric, the drag dipole plays more important role especially when $\alpha \approx 36°$, the drag dipole is strongest. The Strouhal number obtained from this study shows the same trend as reported by Bao, Zhou, and Zhao (2010) and Tu et al. (2014) indicating that the predominant frequency of the generated sound will slowly increase until α reaches 18°. After that, the frequency then rapidly decreases as α is increased.

4.1 Lift and drag coefficients

We first investigate the lift and drag coefficients C_L and C_D, because the fluctuation of lift and drag forces are directly related to the sound generated according to Curle's analogy. Figure 4.1 shows the time histories of lift and drag coefficients of flow past triangular cylinder at Re = 160 for $\alpha = 0°$ and $\alpha = 6°$. From the plot, the fluctuation amplitude of C_L is greater than that of C_D in both figures and it is greater for all incident angle as observed in flow past a circular cylinder (Inoue and Hatakeyama, 2002). This indicates that the fluctuating lift force contributes to the overall sound more than the fluctuating drag force. The period of the C_L is equal to 4.925 and 4.936 for $\alpha = 0°$ and 6°, respectively. The period of the drag coefficient fluctuation is found to be half that of the lift coefficient.

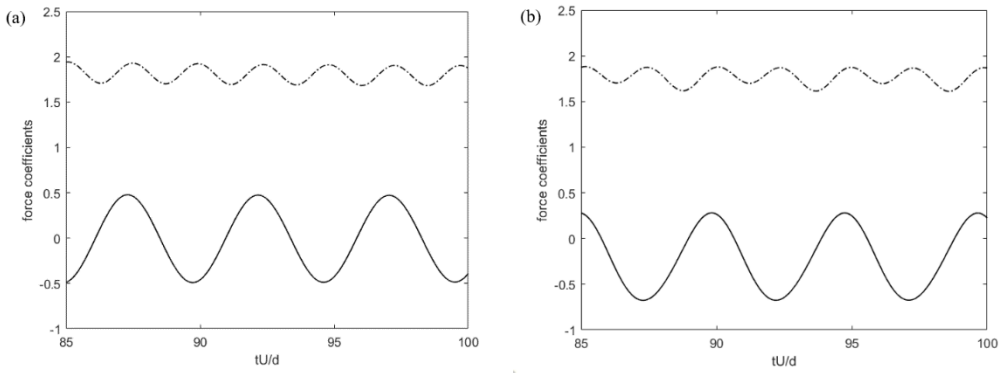

Figure 4.1 Plots of (solid line) lift and (dashed line) drag coefficients of flow past the triangular cylinder at Re =160 at (a) $\alpha = 0°$ and (b) 6°.

Figure 4.2a shows the mean lift coefficient ($C_{L,\text{mean}}$) and mean drag coefficients ($C_{D,\text{mean}}$) as the incident angle is increased at different Reynolds number. The result shows the same trend as reported by Ng et al. (2016) for incompressible flow. The plot shows that $C_{L,\text{mean}}$ is zero when $\alpha = 0°$ and 60° because of the symmetry of the triangular cylinder. From the plot, $C_{L,\text{mean}}$ decreases as α increases to its minimum at $\alpha \approx 30°$ then increases to zero at $\alpha = 60°$. Thus, the averaged downward force is acting to the cylinder for most incident angles. Additionally, the minimum mean lift coefficient found at $\alpha \approx 30°$ indicates that the cylinder is most asymmetric at that $\alpha \approx 30°$. Figure 4.2b shows the mean drag coefficient ($C_{D,\text{mean}}$) at various incident angles and Reynolds numbers. From the result, the trend of $C_{D,\text{mean}}$ decrease when $0° \leq \alpha \leq 24°$ then increases when α is greater than 24°. Ng et al. (2016) suggested that the greater value of $C_{D,\text{mean}}$ at $\alpha = 60°$ than that at $\alpha = 0°$, though the cylinder is both symmetric at both angles, is due to the larger wake developed behind the cylinder. Varying Reynolds number does not significantly affect the trends of mean of both coefficients. For most incident angles, increasing Reynolds number results in a higher drag coefficient for the Reynolds number range in this study.

The root mean square of the lift coefficient ($C_{L,\text{rms}}$) and drag coefficient ($C_{L,\text{rms}}$) centered about its averaged value are shown in Figure 4.3. From the result, $C_{L,\text{rms}}$ gradually increases at increasing α and Re except when $30° \leq \alpha \leq 42°$, $C_{L,\text{rms}}$ is observed to rapidly increase. This implies that the sound generated by the fluctuation of

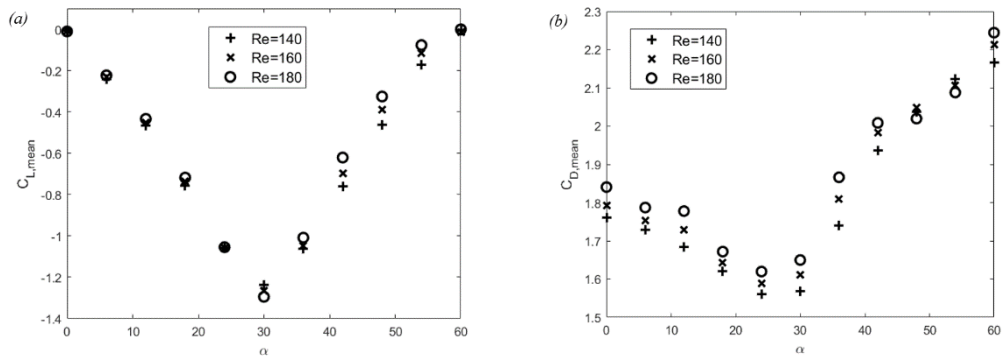

Figure 4.2 Plots of (a) mean lift coefficient and (b) mean drag coefficients of flow past the triangular cylinder.

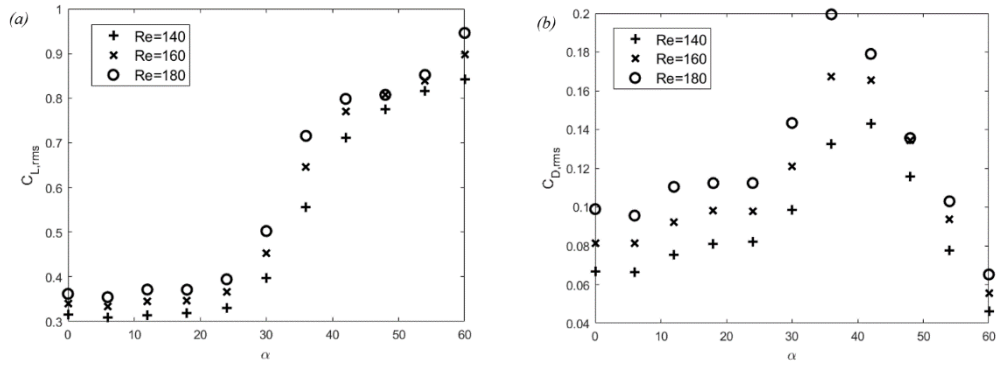

Figure 4.3 Plots of (a) root mean square of lift coefficient and (b) root mean square of drag coefficients of flow past the triangular cylinder.

lift force tend to be louder when the incident angle and Reynolds number are increased and strongest at $\alpha = 60°$. While $C_{D,\mathrm{rms}}$ is found to increase when $0° \leq \alpha \leq 36°$ and decreases when α is approximately bigger than 36°. Even though the mean drag coefficient is found greatest at $\alpha = 60°$, its fluctuation around its mean value is found to be smallest. A higher Re results in a higher $C_{D,\mathrm{rms}}$. This result indicates that the sound generated by the fluctuation of the drag force is strongest at around $36° \leq \alpha \leq 42°$.

Because the sound generated by the fluctuating forces have the same frequency as the fluctuation of forces. We present the plot of power spectral density (PSD) of the lift and drag coefficients in Figure 4.4. From the result, the lift coefficient fluctuates with one main frequency $f \equiv$ St at a time. The very small components of harmonic frequency can also be observed in PSD plot of the lift coefficient. For the drag coefficient, the two frequency components are clearly observed. One has the same

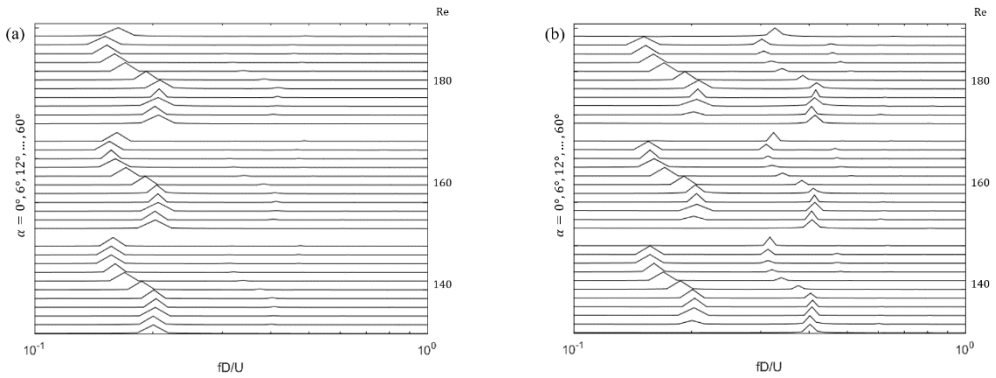

Figure 4.4 Power spectral density of (a) lift coefficient and (b) drag coefficients of flow past triangular cylinder. Each plot has three Reynolds number from (bottom) Re =140, (middle) bottom Re = 160, and (top) Re = 180. In each group of Reynolds number, the incident angle is varied from (bottom) $\alpha = 0°$ to (top) α =60° in increment of 6°. The highest amplitude is normalized to one.

frequency $f_1 =$ St as the lift coefficient. The other one has the frequency twice of the primary frequency $f_2 =$ 2St. Moreover, when the cylinder is symmetric, that is α = 0° and 60°, the drag coefficient oscillates with the frequency $f_2 =$ 2St only. When the cylinder is not symmetric, the frequency $f_1 =$ St is observed in the fluctuation of drag force. From Figure 4.4b, the magnitude of the frequency component $f_1 =$ St grows bigger as α is increased then disappears at α = 60°. Whereas the magnitude of frequency component $f_2 =$ 2St is found to be smallest at α ≈ 42° compared to the frequency f_1 =St.

4.2 Strouhal number

Because the predominant frequency of the sound generated has the same frequency as the frequency of vortex shedding, the Strouhal number St against α at different Re are plotted in Figure 4.5. The result shows the similar trend as reported by Bao, Zhou, and Zhao (2010) and Tu et al. (2014) for incompressible flow. From the result, the Strouhal number is observed to gradually increases when 0° ≤ α ≤ 24° then rapidly decreases when 24° ≤ α ≤ 60°. The maximum St is observed at α ≈ 18° for Re = 140, α ≈ 12° for 160, and α ≈ 24° for Re = 180. The explanation is suggested by Luo

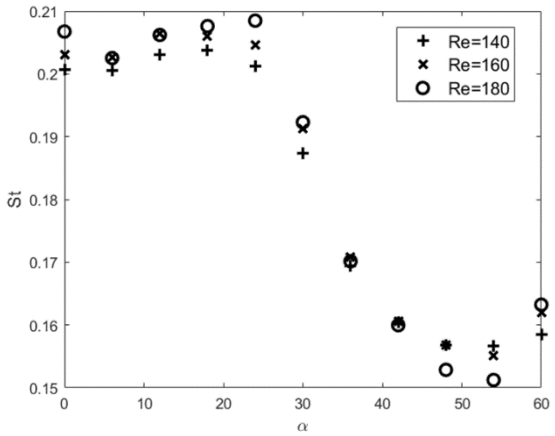

Figure 4.5 The plot of Strouhal number versus incident angle at different Reynolds numbers.

et al. (1994) and Tu et al. (2014) that a small incidence may cause the separated shear layers to reattach onto the rear side of the cylinder, and delay their reaction. By increasing the Reynolds number, the Strouhal number tend to increase except when 36° $\leq \alpha \leq$ 54°.

4.3 Pressure wave generated

In this section, the pressure wave generated by flow past a triangular cylinder is investigated. Figure 4.6 shows the pressure field generated at $\alpha = 36°$ and Re = 160 at non-dimensional time $tU_\infty/d \approx 108$.

Figure 4.7 shows the time histories of the fluctuation pressures at three locations $(r, \theta) = (75d, \pm 90°)$ and $(75d, 180°)$ at $\alpha = 0°$ and 6° at Re = 160 plotted with their force coefficients. The profiles of fluctuation pressure all show the sinusoidal waveforms. The amplitudes of fluctuation pressure at $\theta = \pm 90°$ are greater than that at $\theta = 180°$. Furthermore, the pressure wave at $\theta = 90°$ and $-90°$ is 180° out of phase showing the dipole nature of the sound generated. As the incident angle is increased, the fluctuation pressure at $\theta = 180°$ is observed to deform from the purely-sinusoidal form. While fluctuation pressures at $\theta = \pm 90°$ still retain the sinusoidal forms. The profile of fluctuation pressure at $\theta = 180°$ returns to the sinusoidal form when the cylinder is symmetric again at $\alpha = 60°$. With increasing α, the amplitude of fluctuation pressure is

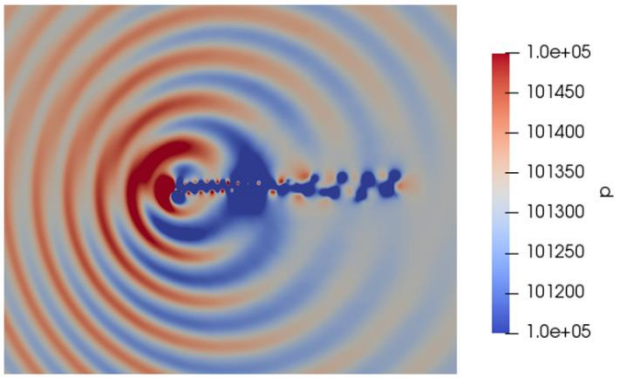

Figure 4.6 The pressure wave generated by flow past triangular cylinder at $\alpha = 36°$ and Re = 160 at non dimensional time $tU_\infty/d = 108$.

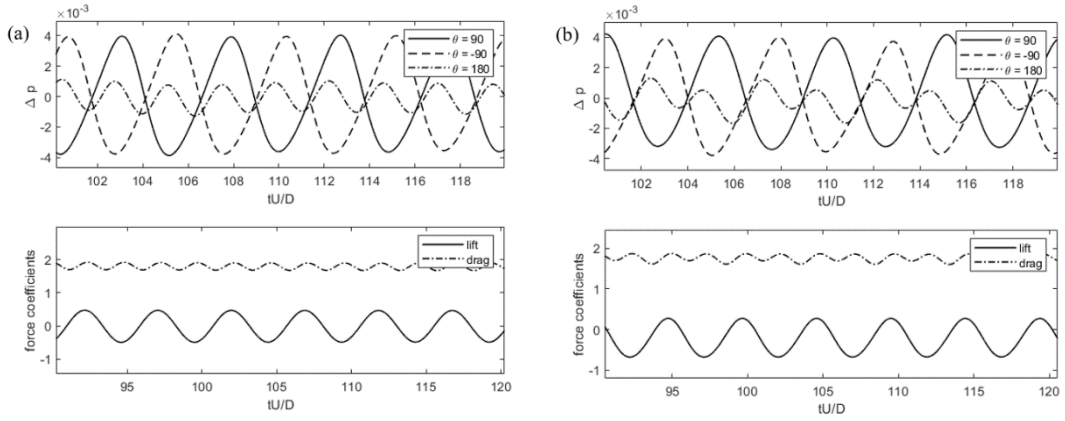

Figure 4.7 Time histories of fluctuation pressure of flow past triangular cylinder when (a) $\alpha = 0°$ and (b) $\alpha = 6°$ for Re = 160 at (r, θ) = $(75d, 0°)$ and $(75d, \pm 90°)$ compare with their force coefficients profiles.

noticed varying. Figure 4.7 shows the fluctuation pressure plotted with their force coefficients. The fluctuation pressures in transverse directions ($\theta = \pm 90°$) and 180° show the similar profiles like their lift and drag coefficients, respectively, according to the Curle's analogy. However, a little difference between the waveform of fluctuation pressure at $\theta = 180°$ and the drag coefficient can be spotted. As seen in Figure 4.7b, both profiles show the doubled-peak waveforms but the second peak of the fluctuation pressure is not as high as that produced in the drag coefficient.

The plots of root mean square of fluctuation pressure against incident angle at different Reynolds numbers are shown in Figure 4.8. Figure 4.8a shows the root mean square of the fluctuation pressure at $(r, \theta) = (75d, 180°)$ showing similar trend as the root mean square of drag coefficient as expected because the sound in front of the

cylinder (in the upstream direction where $y = 0$) is generated mostly by the fluctuation of the drag force. The same reason goes for Figure 4.8b and Figure 4.8c. The plots of root mean square of fluctuation pressure at $(75d, 90°)$ and $(75d, -90°)$ show the similar trends as produced by root mean square of the lift coefficient. However, there is a difference between the sound generated above the cylinder (Figure 4.8b) and below the cylinder (Figure 4.8c). At some incident angles, $\alpha \geq 12°$ for Re = 160, the root mean square of the fluctuation pressure below the cylinder is observed to be greater than that above the cylinder as shown in Figure 4.8d. The biggest difference of the root mean square of fluctuation pressure between the locations above and below the cylinder is found approximately at $\alpha \approx 36°$ for Re = 160.

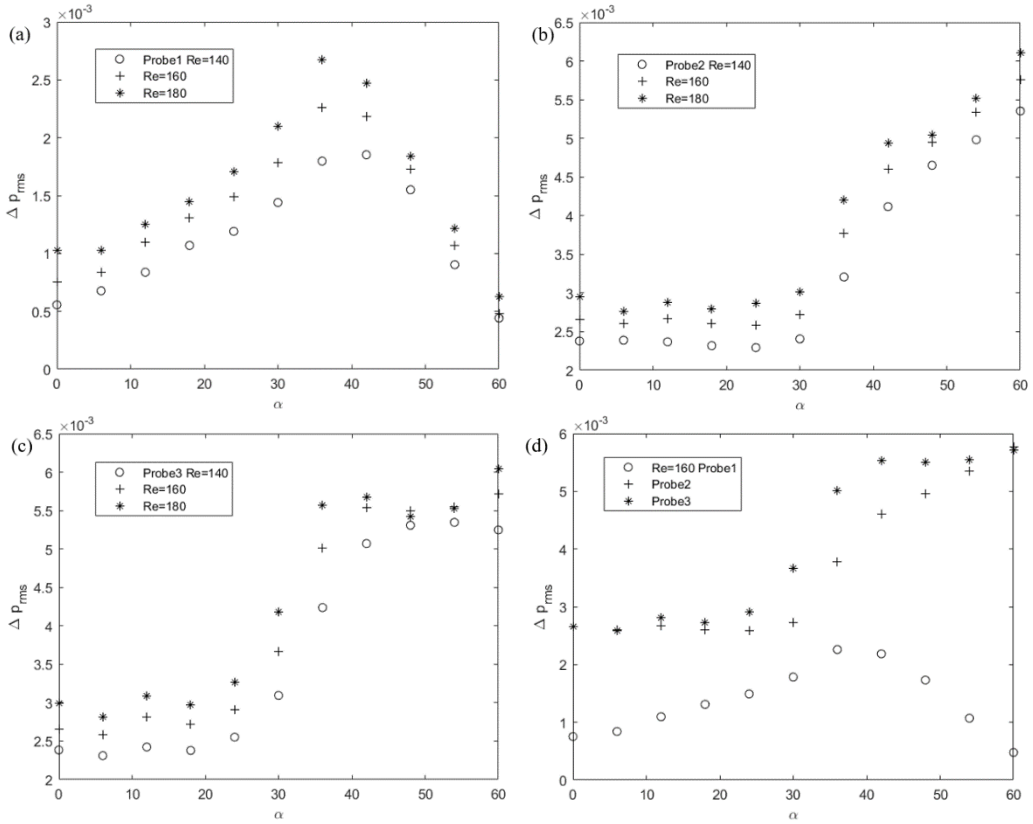

Figure 4.8 Root mean square of fluctuation pressure at each location generated by flow past triangular cylinder. (a) $(r, \theta) = (75d, -180°)$, (b) $(75d, 90°)$, and (c) $(75d, -90°)$ at Re = 140, 160, and 180. (d) Root mean square of fluctuation pressures at three locations when Re = 160. In the legend, probe 1, 2, and 3 are referred to the locations $(75d, 180°)$, $(75d, 90°)$, and $(75d, -90°)$, respectively.

The mean pressure of the fluctuating pressure around the cylinder, though, is not as important as the fluctuating pressure but the result shows that the distribution of the mean pressure around the cylinder is significantly altered when the parameters, especially the incident angle, are varied. Figure 4.9 and Figure 4.10 show the plots of mean pressure of the pressure field around the cylinder at fixed radius $r = 75d$ at Re = 160. As seen in the figures for all incident angles, the mean pressure in the upstream direction is greater than that in the downstream direction. When the cylinder is symmetric, the mean pressures above and below the cylinder show the comparable result due to its symmetric configuration. Unlike when the cylinder is asymmetric, the mean pressures above and below the cylinder show the differences value both in value and trend. The mean pressure on the upper half plane shows the greater value than that observed in the symmetric case. On the other hand, the mean pressure below the asymmetric cylinder is observed to be smaller than that in the symmetric case, thus results in a downward force acting on the cylinder as seen in Section 1. The difference in mean pressure at the same vertical line $(\theta = -\theta)$ is found increasing when the incident angle is increased. The maximum difference in mean pressure is approximately found at $\alpha \approx 30^\circ - 36^\circ$ then decreases afterwards. The distribution of mean pressure is not significantly affected by increasing the Reynolds number as seen in Figure 4.11.

One of the purposes of this study is to find the sound generated from the other sources not only generated from the fluctuation of force acting on the cylinder but also the sound generated by the secondary vortex street as observed in Inasawa et al. (2013). From the result shown in Figure 4.12, the sound generated have only the frequency component equal to its primary Strouhal number, twice of primary Strouhal number, or its harmonics. This indicates that the sound is generated mainly from the fluctuation of force acting on the cylinder. The monopole sound source generated from the fluctuating mass with the frequency equal twice of vortex shedding frequency may also contribute to the overall sound but this is not in the goal of this study. The sound from the secondary vortex street may be generated due to its presented in the flow field but may not be strong enough to propagate to the probe location so we did not observe that kind of sound. The sound generated is expected to have more frequency components as the Reynolds number is increased. For instance, when the Reynolds number reaches 200, more frequency peaks are observed in the PSD of the lift

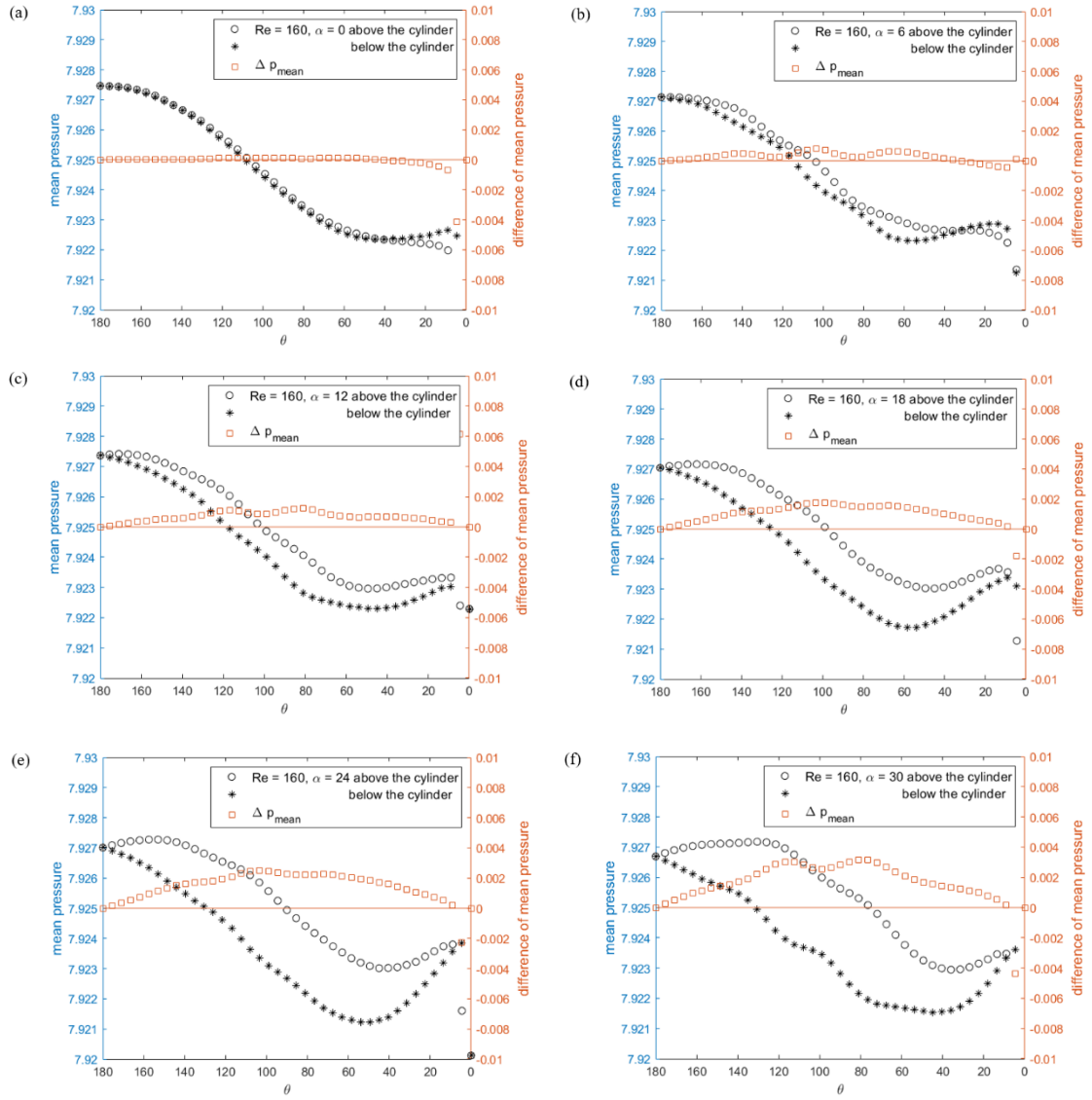

Figure 4.9 Left axis represents mean pressure distribution around the triangular cylinder at (a)-(f) $\alpha = 0°,6°,...,30°$ for Re = 160. Right axis represents the difference in mean pressure between above and below the cylinder at the same θ

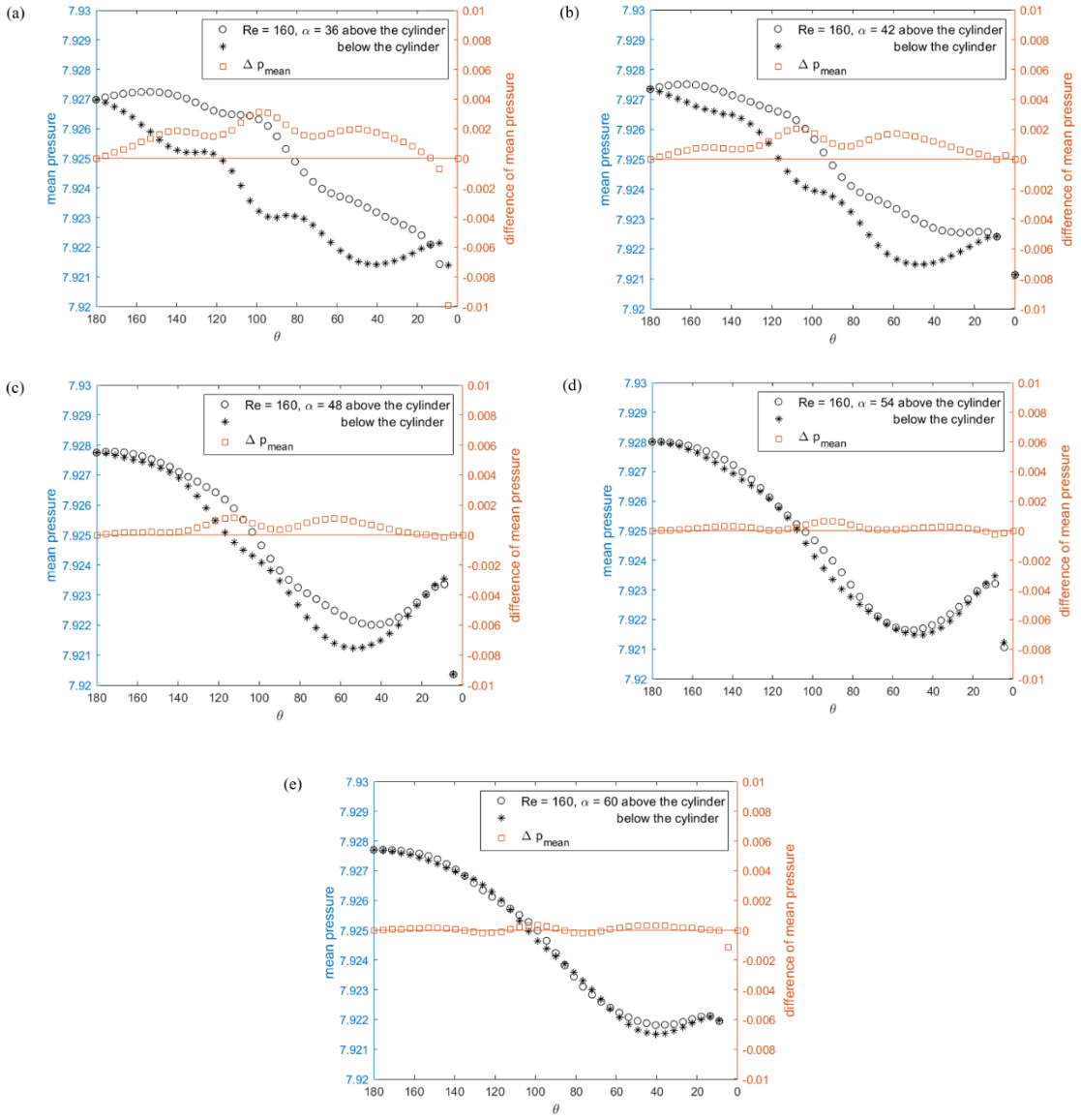

Figure 4.10 Left axis represents mean pressure distribution around the triangular cylinder at (a)-(e) $\alpha = 36°,42°,...,60°$ for Re = 160. Right axis represents the difference in mean pressure between above and below the cylinder at the same θ.

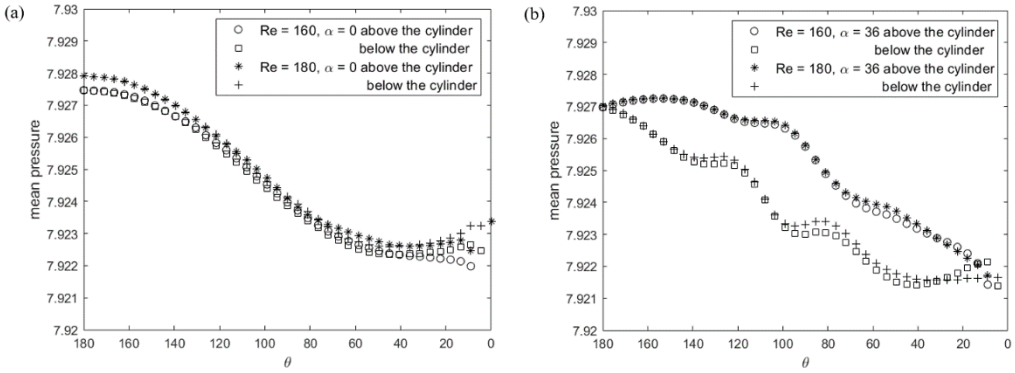

Figure 4.11 Mean pressure distribution around the triangular cylinder at (a) α =0° and (b) α = 36° for Re = 160 and 180.

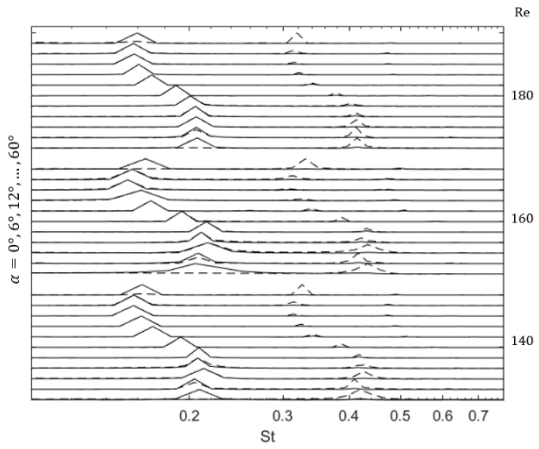

Figure 4.12 The spectrum of the sound generated from flow past triangular cylinder at various incident angles and Reynolds numbers at (solid line) $(r, \theta) = (75d, 90°)$ and (dashed line) $(75d, 180°)$. In each group of Reynolds number, the incident angle is varied from (bottom) $\alpha = 0°$ to (top) $\alpha = 60°$ in increment of 6°. The highest amplitude is normalized to one.

coefficient but with smaller amplitude than its primary Strouhal number as reported by Ng et al. (2016). Therefore, that would result in the more frequency components in the sound generated.

To study the decay of the pressure wave generated, the pressure field are collected at different distance from $r = 10d$ to $r = 100d$ at $\theta = \pm 90°$. The plot of root mean square of fluctuation pressure when the cylinder is symmetric, $\alpha = 60°$ and Re = 140 is chosen, and when the cylinder is asymmetric, $\alpha = 36°$ and Re = 160 is chosen, is presented in Figure 4.13. From the figure, the root mean square of the pressure

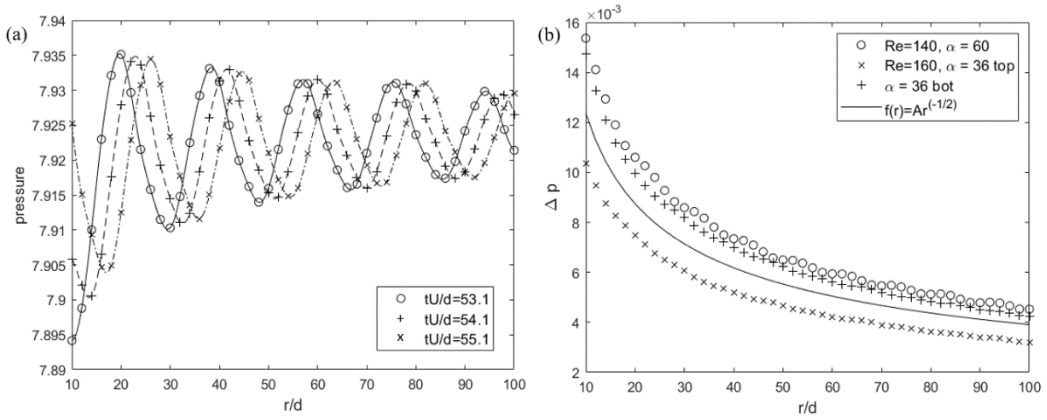

Figure 4.13 The plot of fluctuation pressure against the distance r showing the decay of the fluctuation pressure. (a) The pressure wave at different distance r at three non-dimensional time. (b) Decay of the fluctuation pressure. The words 'top' and 'bot' in the right figure are referred to θ =90° and −90°, respectively.

fluctuation clearly decays as $r^{-1/2}$ for the pressure wave generated by both cases of the cylinder.

The directivity plots of the root mean square of fluctuation pressure are shown in Figure 4.14 and Figure 4.15. From the result, when the incident angle $\alpha = 0°$, the purely dipole field is observed in the pressure field. This dipole field is generated in the same manner as that generated in flow past circular cylinder by Inoue and Hatakeyama (2002). The direction of the dipole is approximately $\pm$100° to the flow direction. The bending angle of the dipole's direction from 90° is a result of the Doppler effect as mentioned in Inoue and Hatakeyama (2002). This indicates that the sound field is dominated by the lift dipole. With increasing α, the pressure field starts to deform from a purely dipole field. When the incident angle $\alpha = 36°$ shown in Figure 4.15e, the root mean sqaure of fluctuation pressure at the lower side of the cylinder is observed greater than that generated at the upper side. The maximum $\Delta\tilde{p}$ on the half upper side is found in the upstream direction at $\theta \approx 67.5°$, whereas that of the half lower side is found in the downstream direction at $\theta \approx -99°$. At $\alpha = 18°$, the root mean square of fluctuation pressure at $\theta \approx -165°$ shows the greater value than generated at small incident angles and is observed to grow bigger with increasing α. When α reaches 30°, the root mean square of fluctuation pressure is observed to be much greater than that generated when the incident angle is small especially in the upstream direction. The

direction of the dipole is observed to start bending to the downstream direction in the upper half plane. At $\alpha = 42°$, the pressure field is observed to start deforming back to the dipole field. The minimum of $\Delta\tilde{p}_{\mathrm{rms}}$ in the upstream direction is observed at $\alpha \approx 165°$. Additionally, the maximum $\Delta\tilde{p}_{\mathrm{rms}}$ at the lower half of the domain under the cylinder is observed to be significantly greater than that on the upper side of the cylinder. The direction of the dipole is approximately 75° and 255° in the upper and lower sides, respectively. When the cylinder returns back to the symmetric configuration, $\alpha = 60°$, the dipole field is clearly observed again. Therefore, the clearly-observed dipole field is generated when the cylinder is symmetric due to the symmetry of the bluff body and small fluctuating drag force compared to that of the lift force. When the cylinder is asymmetric, the root mean square of fluctuation pressure shows the shape deforming form the dipole field as a result of higher fluctuating drag force. At some incident angles, the maximum of $\Delta\tilde{p}_{\mathrm{rms}}$ is observed in the downstream direction on the upper half plane and in the upstream direction in the lower half plane. The higher root mean square of fluctuation pressure at $\alpha = 60°$ than that at $\alpha = 0°$ is caused by the higher fluctuation in lift coefficient. Therefore, the pressure field generated is affected mainly by the incident angle of the triangular cylinder for the Reynolds number in this study range.

4.4 Vortex street and characteristics of the wake

The pattern of the vortex street developed behind the triangular cylinder at different incident angles and at Reynolds numbers between 80 and 200 of incompressible flow is reported by Ng et al. (2016) to exhibit five patterns. Figure 4.6 shows the map of different vortex streets exhibited by unsteady flow. In the figure, regime (I) represents the Bénard-von Kármán vortex street, regime (II) shows the bi-layered wake arrangement, regime (III) shows the secondary vortex street, regime (IV) and (V) represent the *P*+*S*-like wake and *2P*-like wake, respectively. Table 4.1 summarizes the pattern of the nearest vortex street developed by the flow past triangular cylinder.

At Reynolds number 140, the Bénard-von Kármán vortex street is observed near the cylinder. The Bénard-von Kármán vortex street then rearranges into two layers

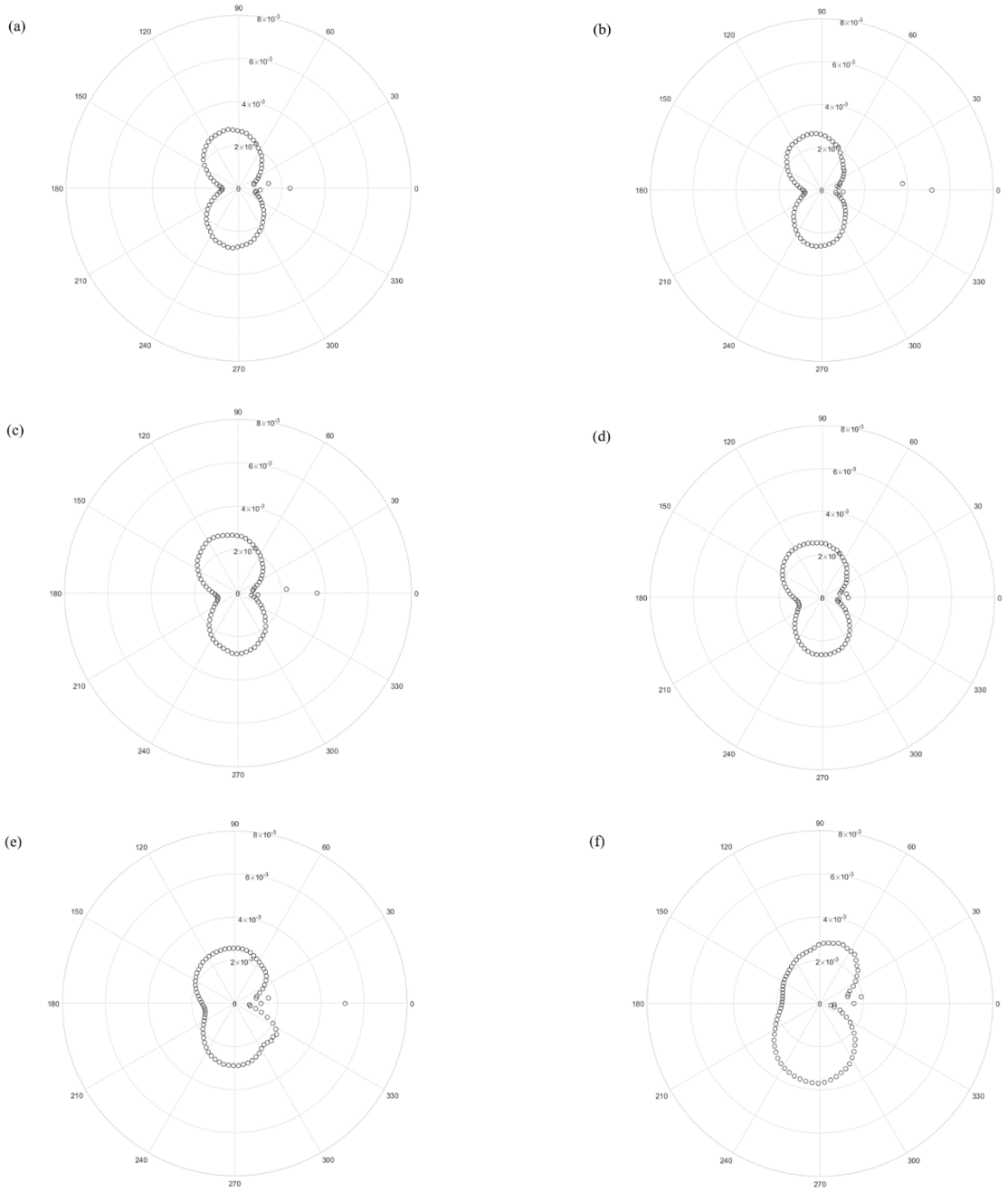

Figure 4.14 Directivity plot of root mean square of fluctuation pressure at incident angles (a)-(f) 0°,6°,...,30° at Re = 160.

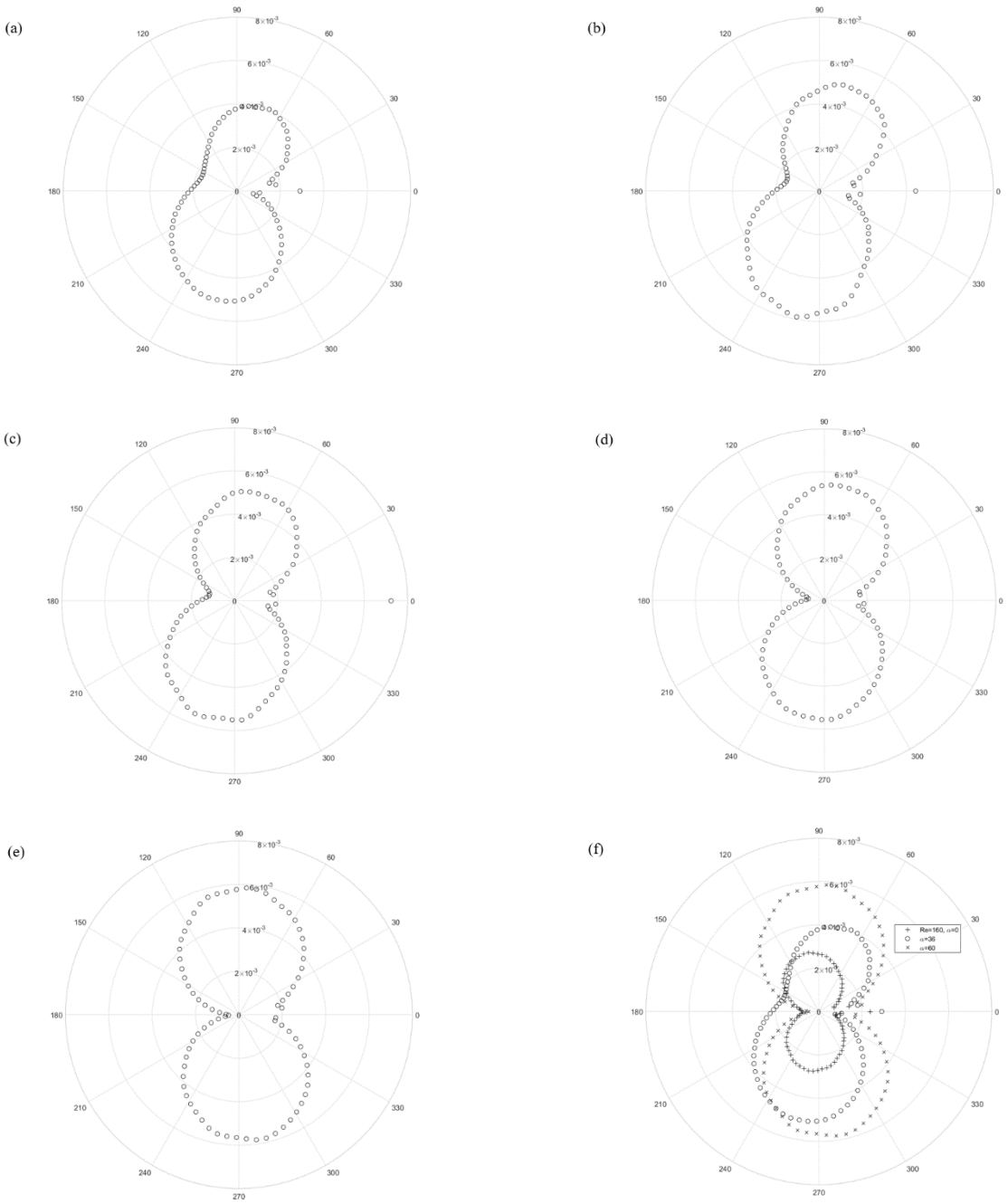

Figure 4.15 Directivity plot of root mean square of fluctuation pressure at incident angles (a)-(e) 36°,42°,...,60° at Re = 160. (f) Directivity plot of root mean square of fluctuation pressure at α =0°, 36°, and 60° at Re = 160.

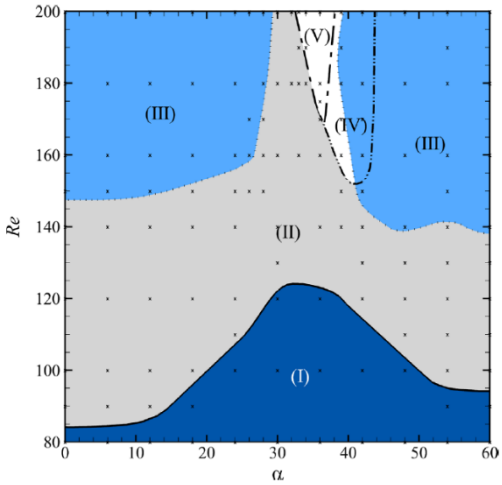

Figure 4.16 Map of different vortex street developed by flow past triangular cylinder at different incident angles between the Reynolds number 80 - 200. After Ng et al. (2016).

of vortices with different signs. The negative and positive signs of vortices' rows are at upper and lower sides of the domain, respectively. The two layers of vortices then reform into another vortex street with bigger scale and advected downstream. The amount of vortices before turning into bi-layered wake is observed to be different when the incident angles is varied. The maximum amount of vortices is observed at α between 30° and 36°. The length of bi-layers wake is also observed to be different before reforming into a secondary vortex street. The shortest bi-layers wakes are observed at $\alpha = 0°$ and 36°. These results (Re = 140) are different from those reported by Ng et al. (2016) in that most incident angles (except $\alpha = 48°$ and 60°) give a bi-layers wake arrangement. The possible explanation for this contradiction would be the domain's length of Ng et al. (2016) may not be large enough for the transformation of bi-layers wake into the secondary vortex street. The similar wake characteristics are observed in flows at Reynolds number 160. When the cylinder is inclined at $42° \leq \alpha \leq 54°$, the small vortices with positive sign above the layer of negative vortices are noticed to be stronger in magnitude than at other incident angles as shown in Figure 4.17 indicating that the *P*+*S*-like wake is generated at this angle. At Reynolds number 180, most incident angles still exhibit the Bénard-von Kármán vortex street, the bi-layered wake, and the secondary vortex street. The *P*+*S*-like wake can be also observed at incident angle between 42° and 54° as shown in Figure 4.17. In this study, what we observe is that all parameters in this study range give the secondary vortex street in the wake.

Table 4.1 The pattern of the vortex street nearest to the triangular cylinder at different incident angles and Reynolds number. The BK and P+S stand for the Bénard-von Kármán vortex street and the *P*+*S*-like wake, respectively.

Reynolds number	0°	6°	12°	18°	24°	30°	36°	42°	48°	54°	60°
140	BK	BK	BK	BK	BK	BK	BK	BK	BK	BK	BK
160	BK	BK	BK	BK	BK	BK	BK	P+S	P+S	P+S	BK
180	BK	BK	BK	BK	BK	BK	BK	P+S	P+S	P+S	BK

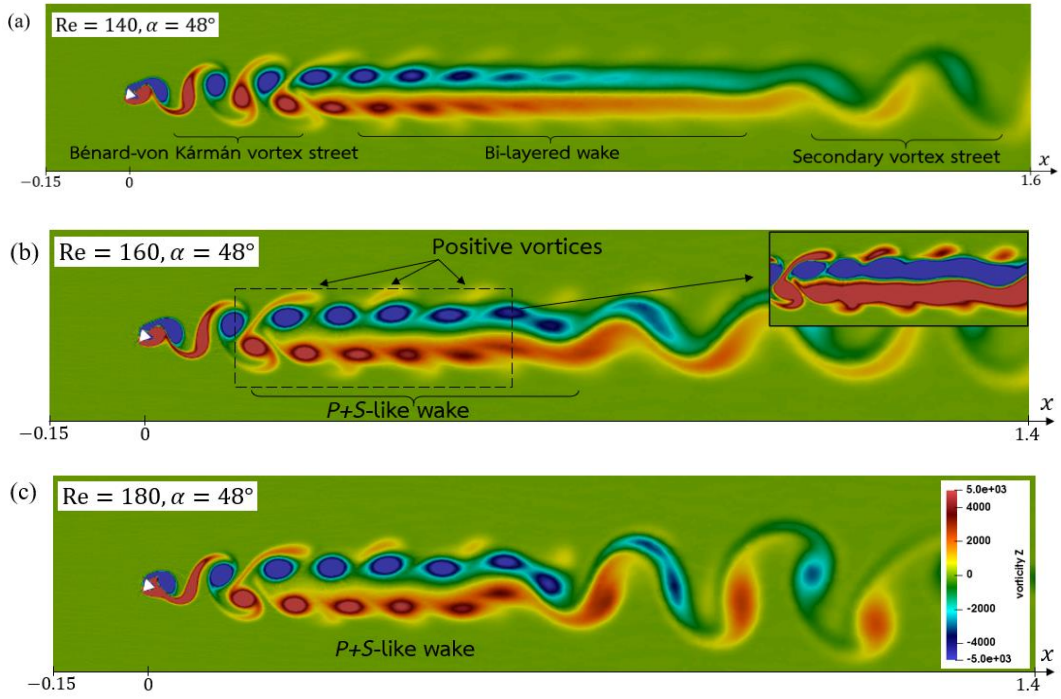

Figure 4.17 Vorticity field of flow past triangular cylinder at (a) Re = 140 and $\alpha = 48°$, (b) Re = 160 and $\alpha = 48°$, and (c) Re = 180 and $\alpha = 48°$.

CHAPTER V
CONCLUSION

In this thesis, we study the sound generated and wake characteristics of flow past an equilateral triangular cylinder at different incident angles and Reynolds numbers. Because at low Reynold number the sound is generated mostly from the fluctuation of lift and drag forces, we first investigate the lift and drag coefficients.

The results of the lift and drag coefficients show that their mean values vary mostly as a function of incident angle at the Reynolds numbers in this study range. The mean value of the lift coefficient vanishes when the cylinder is symmetric to the incoming flow. The mean lift coefficient decreases as the incident angles is increased and reaches its minimum at the incident angles approximately 30° then increased afterward. For the mean drag coefficient, it is found to decrease with increasing incident angle until the incident angle reaches, approximately, 24° then increases as the incident angle increases afterward.

However the mean values of the lift and drag coefficients are not directly related to the sound induced by the flow, but the root mean square of the lift and drag coefficients are. The root mean square of the lift coefficient shows that it is relatively small when the incident angle is small (especially when $\alpha \leq 18°$) and grow bigger rapidly at $24° \leq \alpha \leq 42°$ and still increase as the incident angle is increased. This can imply that the sound generated from the fluctuation of the lift force gets louder with increasing incident angle and it is amplified more than two times when the incident angle is small. For the root mean square of the drag coefficient, its value is normally small compared to that of the lift coefficient. The sound induced by the fluctuation of the drag force is a smaller part to the overall sound generated. From the result, the root mean square of the drag coefficient is found to increase when the incident angle is increased until reach its maximum at incident angle approximately 36° - 42° then decreases afterwards. This shows that the sound generated from the fluctuation of drag force is strongest at incident angles around 36° - 42°. Increasing the Reynolds number

does not significantly affect the trends of the mean values and the root mean square values of both coefficients but gives a greater or lower value for the Reynolds number in this study.

For the frequency of the sound generated, two frequencies play an important role in a flow field. One has the frequency of the vortex shedding (and the same with the frequency of the lift coefficient) mostly generated from the fluctuation of the lift force. Another sound source with the frequency of vortex shedding is the fluctuation of the drag coefficient which is generated when the cylinder is asymmetric. Second has the frequency twice that of the vortex shedding generated mostly from the fluctuation of the drag coefficient. This frequency is most pronounced when the cylinder is symmetric. When the incident angle is small, the Strouhal number has a value of around 0.21. With increasing incident angle, the frequency of vortex shedding is observed varying. The frequency of the vortex shedding is observed to slightly increase as the incident angle increases (by 1.48%) when the incident angle is less than, approximately, 18°- 24° then rapidly decrease at increasing incident angle (by 24.8% at $\alpha = 54°$). The frequency is found to increase again by 4.52% at an incident angle of 60°. Increasing the Reynolds number does not significantly affect on the trend on the frequency of vortex shedding for the Reynolds number in this study.

The results on the sound pressure wave generated in upstream and transverse directions show that the sound field is mostly produced by the fluctuation of the lift and drag forces acting on the cylinder. The monopole sound source with the frequency twice the frequency of the vortex shedding generated from the fluctuating mass may also contribute to the acoustic field. The pressure wave induced by the flow is observed to decay as propagating away from the cylinder following the inverse square law. The root mean squares of the pressure wave in the upstream and the transverse directions have the same trends as the root mean squares of the drag and the lift coefficients, respectively. The root mean square of the pressure wave in the upstream direction increases with increasing incident angle until at an incident angle of around 36° (increases by 159%) then decreases afterwards (decreases by 76%). As the incident angle is increased, the root mean square of the pressure wave in the transverse direction increases (by 115% at $\alpha = 60°$). When the cylinder is asymmetric, the root mean square of the fluctuation pressure below the cylinder is found to be greater than that on the

upper side (by around 28% at $\alpha = 36°$). This may be caused by the monopole sound source. The results on the mean pressure distribution are presented showing that when the cylinder is asymmetric the mean pressure around the cylinder on the upper side is greater than on the lower side. The maximum difference of the mean pressure is found at the incident angle 30°- 36°.

For the pattern of the wake developed by flow past the triangular cylinder, there are two types of the wake observed in this study. One is the Bénard-von Kármán vortex street observed to develop for most parameters in this study. Two is the *P+S*-like wake observed at the incident angle between 42° and 54° for the Reynolds number 160 and 180. Most of the case with the Bénard-von Kármán vortex street turns into, respectively, the biyered-wake and the secondary vortex street as advecting downstream. Whereas the *P+S*-like wake having the characteristics similar to the bi-layered wake arrangement itself turns into, also, the secondary vortex street. The *2P*-like wake observed in Ng et al. (2016) is not found in this study, for the selected parameters, and may be caused by the size of the computational domain or the different governing equations.

REFERENCES

1 Lighthill MJ. On sound generated aerodynamically I. General theory. Proceedings of the Royal Society of London. Series A. Mathematical and Physical Sciences. 1952 Mar 20;211(1107):564-87.

2 Curle N. The influence of solid boundaries upon aerodynamic sound. Proceedings of the Royal Society of London. Series A. Mathematical and Physical Sciences. 1955 Sep 20;231(1187):505-14.

3 Blevins RD. Review of sound induced by vortex shedding from cylinders. Journal of Sound and Vibration. 1984 Feb 22;92(4):455-70.

4 Fujita H, Sha W, Furutani H, Suzuki H. Experimental investigations and prediction of aerodynamic sound generated from square cylinders. In4th AIAA/CEAS Aeroacoustics Conference 1998 (p. 2369).

5 Doolan C. Flow and noise simulation of the NASA tandem cylinder experiment using OpenFOAM. In15th AIAA/CEAS Aeroacoustics Conference (30th AIAA Aeroacoustics Conference) 2009 May 11 (p. 3157).

6 Fujita H. The characteristics of the Aeolian tone radiated from two-dimensional cylinders. Fluid dynamics research. 2010 Jan 18;42(1):015002.

7 Lysenko DA, Ertesvåg IS, Rian KE. Towards simulation of far-field aerodynamic sound from a circular cylinder using OpenFOAM. International Journal of Aeroacoustics. 2014 Apr;13(1-2):141-68.

8 Oguma Y, Fujisawa N. Sound source measurement of a semi-circular cylinder in a uniform flow by particle image velocimetry. Journal of Flow Control, Measurement & Visualization. 2016 Sep 13;4(4):162-70.

9 Inoue O, Hatakeyama N. Sound generation by a two-dimensional circular cylinder in a uniform flow. Journal of Fluid Mechanics. 2002 Nov 1;471:285.

10 Liow YS, Tan BT, Thompson MC, Hourigan K. Sound generated in laminar flow past a two-dimensional rectangular cylinder. Journal of Sound and Vibration. 2006 Aug 8;295(1-2):407-27.

11 Inoue O, Mori M, Hatakeyama N. Aeolian tones radiated from flow past two square cylinders in tandem. Physics of Fluids. 2006 Apr 6;18(4):046101.

12 Inoue O, Iwakami W, Hatakeyama N. Aeolian tones radiated from flow past two square cylinders in a side-by-side arrangement. Physics of Fluids. 2006 Apr 20;18(4):046104.

13 Inasawa A, Asai M, Nakano T. Sound generation in the flow behind a rectangular cylinder of various aspect ratios at low Mach numbers. Computers & Fluids. 2013 Aug 15;82:148-57.

14 Mat Ali MS, Doolan CJ, Wheatley V. Low Reynolds number flow over a square cylinder with a splitter plate. Physics of Fluids. 2011 Mar 31;23(3):033602.

15 Sandberg RD, Jones LE, Sandham ND, Joseph PF. Direct numerical simulations of tonal noise generated by laminar flow past airfoils. Journal of Sound and Vibration. 2009 Mar 6;320(4-5):838-58.

16 Margnat F. Hybrid prediction of the aerodynamic noise radiated by a rectangular cylinder at incidence. Computers & Fluids. 2015 Mar 10;109:13-26.

17 Bao Y, Zhou D, Zhao YJ. A two-step Taylor-characteristic-based Galerkin method for incompressible flows and its application to flow over triangular cylinder with different incidence angles. International journal for numerical methods in fluids. 2010 Apr 20;62(11):1181-208.

18 Tu J, Zhou D, Bao Y, Han Z, Li R. Flow characteristics and flow-induced forces of a stationary and rotating triangular cylinder with different incidence angles at low Reynolds numbers. Journal of Fluids and Structures. 2014 Feb 1;45:107-23.

19 Ng ZY, Vo T, Hussam WK, Sheard GJ. Two-dimensional wake dynamics behind cylinders with triangular cross-section under incidence angle variation. Journal of Fluids and Structures. 2016 May 1;63:302-24.

20 Mat Ali MS, Shaikh Salim SA, Ismail MH, Muhamad S, Mahzan MI. Aeolian tones radiated from flow over bluff bodies. The Open Mechanical Engineering Journal. 2013 Oct 18;7(1).

21 Glegg S, Devenport W. Aeroacoustics of low Mach number flows: fundamentals, analysis, and measurement. Academic Press; 2017 Feb 15.

22 Kundu PK, Cohen IM, Dowling D. Fluid Mechanics 4th.

APPENDICES

APPENDIX A

Dynamic viscosity

The dynamic viscosities used for each incident angle and Reynolds number are given in Table A.1

Table A.1 The dynamic viscosities used for each incident angle and Reynolds number ($\times 10^{-2}$ kg/(m×s))

α \ Re	140	160	180
0°	1.771	1.550	1.377
6°	1.761	1.541	1.370
12°	1.732	1.516	1.347
18°	1.684	1.474	1.310
24°	1.618	1.416	1.258
30°	1.534	1.342	1.193
36°	1.618	1.416	1.258
42°	1.684	1.474	1.310
48°	1.732	1.516	1.347
54°	1.761	1.541	1.370
60°	1.771	1.550	1.377

APPENDIX B

Geometry file

The geometry file of a triangular cylinder in a square domain created by Gmsh for an incident angle of 0°.

```
// Gmsh project created on Mon Jun 10 19:24:51 2019
SetFactory("OpenCASCADE");
//+
Point(1) = {620, 620, -0.5, 0.25};
//+
Point(2) = {620, -620, -0.5, 0.25};
//+
Point(3) = {-620, -620, -0.5, 0.25};
//+
Point(4) = {-620, 620, -0.5, 0.25};
//+
Point(5) = {-1.1547, 0, -0.5, 0.003};
//+
Point(6) = {0.57735, 1, -0.5, 0.003};
//+
Point(7) = {0.57735, -1, -0.5, 0.003};
//+
Line(1) = {6, 7};
//+
Line(2) = {7, 5};
//+
```

```
Line(3) = {5, 6};
//+
Line(4) = {4, 1};
//+
Line(5) = {1, 2};
//+
Line(6) = {2, 3};
//+
Line(7) = {3, 4};
//+
Line Loop(1) = {4, 5, 6, 7};
//+
Line Loop(2) = {3, 1, 2};
//+
Plane Surface(1) = {1, 2};
//+
Extrude {0, 0, 1} {
  Surface{1};
  Layers{1};
  Recombine;
}
//+
Physical Surface("top") = {2};
//+
Physical Surface("out") = {3};
//+
Physical Surface("bot") = {4};
//+
Physical Surface("in") = {5};
```

```
//+
Physical Surface("cylinder") = {6, 7, 8};
//+
Physical Surface("frontAndBack") = {9, 1};
//+
Physical Volume(7) = {1};
```

APPENDIX C
OpenFOAM file

In running a case in OpenFOAM, there are three important directories. First is directory ‘0’ containing the initial value of variables being solved (pressure, velocity, and temperature in this study). Second is directory ‘constant’ containing the properties that are constant in the simulation. Third is directory ‘system’ containing methods or scheme of the numerical solver being used. Given below are the pressure, velocity, and temperature in directory ‘0’, ‘thermophysicalProperties’ in directory constant, and ‘controlDict’ in directory system of flow past triangular cylinder at an incident angle of 0° at Re = 160.

Pressure file

```
/*---------------------------------*- C++ -*----------------------------------*\
| =========                 |                                                 |
| \\      /  F ield         | OpenFOAM: The Open Source CFD Toolbox           |
|  \\    /   O peration     | Version:  5.x                                   |
|   \\  /    A nd           | Web:      www.OpenFOAM.org                      |
|    \\/     M anipulation  |                                                 |
\*---------------------------------------------------------------------------*/
FoamFile
{
    version     2.0;
    format      ascii;
    class       volScalarField;
    location    "0";
    object      p;
```

```
}
// * * * * * * * * * * * * * * * * * * * * * * * * * * * * * * * * * * * * * * * * * * * * //
dimensions      [1 -1 -2 0 0 0 0];
internalField   uniform 101325;
boundaryField
{
    in
    {
        type            zeroGradient;
    }
    top
    {
        type            zeroGradient;
    }
    bot
    {
        type            zeroGradient;
    }
    out
    {
        type            waveTransmissive;
        gamma           1.3999999999999999112;
        fieldInf        101325;
        lInf            1;
        value           uniform 101325;
    }
    cylinder
    {
        type            zeroGradient;
```

```
    }
    frontAndBack
    {
        type            empty;
    }
}
//
********************************************************************
**** //
```

Velocity file

```
/*--------------------------------*- C++ -*----------------------------------*\
| =========                 |                                                 |
| \\      /  F ield         | OpenFOAM: The Open Source CFD Toolbox           |
|  \\    /   O peration     | Version:  5.x                                   |
|   \\  /    A nd           | Web:      www.OpenFOAM.org                      |
|    \\/     M anipulation  |                                                 |
\*---------------------------------------------------------------------------*/
FoamFile
{
    version     2.0;
    format      ascii;
    class       volVectorField;
    location    "0";
    object      U;
}
// * * * * * * * * * * * * * * * * * * * * * * * * * * * * * * * * * * * * * //

dimensions      [0 1 -1 0 0 0 0];
internalField   uniform (1.0314e+02 0 0);
```

```
boundaryField
{
    in
    {
        type            fixedValue;
        value           uniform (1.0314e+02 0 0);
    }
    top
    {
        type            fixedValue;
        value           uniform (1.0314e+02 0 0);
    }
    bot
    {
        type            fixedValue;
        value           uniform (1.0314e+02 0 0);
    }
    out
    {
        type            inletOutlet;
        inletValue      uniform (0 0 0);
        value           uniform (0 0 0);
    }
    cylinder
    {
        type            fixedValue;
        value           uniform (0 0 0);
    }
    frontAndBack
```

```
    {
        type            empty;
    }
}
//
********************************************************************************
**** //
```

Temperature file

```
/*--------------------------------*- C++ -*----------------------------------*\
| =========                 |                                                 |
| \\      /  F ield         | OpenFOAM: The Open Source CFD Toolbox           |
|  \\    /   O peration     | Version:  5.x                                   |
|   \\  /    A nd           | Web:      www.OpenFOAM.org                      |
|    \\/     M anipulation  |                                                 |
\*---------------------------------------------------------------------------*/
FoamFile
{
    version     2.0;
    format      ascii;
    class       volScalarField;
    location    "0";
    object      T;
}
// * * * * * * * * * * * * * * * * * * * * * * * * * * * * * * * * * * * * * * * * //

dimensions      [0 0 0 1 0 0 0];
internalField   uniform 293.14999999999997726;
boundaryField
{
```

```
in
{
    type            fixedValue;
    value           uniform 293.14999999999997726;
}
top
{
    type            fixedValue;
    value           uniform 293.14999999999997726;
}
bot
{
    type            fixedValue;
    value           uniform 293.14999999999997726;
}
out
{
    type            inletOutlet;
    inletValue      uniform 293.14999999999997726;
    value           uniform 293.14999999999997726;
}
cylinder
{
    type            zeroGradient;
}
frontAndBack
{
    type            empty;
}
```

```
}
//
*********************************************************************
**** //
```

thermophysicalProperties file

```
/*---------------------------------*- C++ -*----------------------------------*\
| =========                 |                                                 |
| \\      /  F ield         | OpenFOAM: The Open Source CFD Toolbox           |
|  \\    /   O peration     | Version:  4.x                                   |
|   \\  /    A nd           | Web:      www.OpenFOAM.org                      |
|    \\/     M anipulation  |                                                 |
\*---------------------------------------------------------------------------*/
FoamFile
{
    version     2.0;
    format      ascii;
    class       dictionary;
    object      thermophysicalProperties;
}
// * * * * * * * * * * * * * * * * * * * * * * * * * * * * * * * * * * * * * //
thermoType
{
    type            hePsiThermo;
    mixture         pureMixture;
    transport       const;
    thermo          hConst;
    equationOfState perfectGas;
    specie          specie;
    energy          sensibleEnthalpy;
```

```
}
mixture
{
   specie
   {
      nMoles      1;
      molWeight   28.9;
   }
   thermodynamics
   {
      Cp          1005;
      Hf          0;
   }
   transport
   {
      mu          0.01550; // for D=0.02
      Pr          0.713;
   }
}
//
*********************************************************************
**** //
```

controlDict file

```
/*--------------------------------*- C++ -*----------------------------------*\
| =========                 |                                                 |
| \\      /  F ield         | OpenFOAM: The Open Source CFD Toolbox           |
|  \\    /   O peration     | Version:  4.x                                   |
|   \\  /    A nd           | Web:      www.OpenFOAM.org                      |
|    \\/     M anipulation  |                                                 |
\*---------------------------------------------------------------------------*/
```

```
FoamFile
{
   version     2.0;
   format      ascii;
   class       dictionary;
   object      controlDict;
}
// * * * * * * * * * * * * * * * * * * * * * * * * * * * * * * * * * * * * * * * * //
application     rhoPimpleFoam;
startFrom       latestTime;
startTime       0;
stopAt          endTime;
endTime         0.028;
deltaT          0.000001;
writeControl    adjustableRunTime;
writeInterval   0.007;
purgeWrite      0;
writeFormat     ascii;
writePrecision  20;

writeCompression off;
timeFormat      general;
timePrecision   6;
runTimeModifiable true;
adjustTimeStep  yes;
maxCo           0.6;
maxDeltaT       1;
//
************************************************************************
**** //
```

```
functions
{
   fieldAverage
   {
      type          fieldAverage;
      functionObjectLibs ("libfieldFunctionObjects.so");
      enabled       true;
      writeControl   outputTime;
      fields
      (
         U
         {
            mean       on;
            prime2Mean  off;
            base       time;
         }
         p
         {
            mean       on;
            prime2Mean  off;
            base       time;
         }
         T
         {
            mean       on;
            prime2Mean  off;
            base       time;
         }
      );
```

```
    }
////////////////////////////////////////////////////////////////////////////
////////////////////////////////////////////////////////////////////////////
    forces_object
    {
        type forces;
        functionObjectLibs ("libforces.so");
        writeControl   timeStep;
        writeInterval  1;
        //// Patches to sample
        patches ("cylinder");
        //// Name of fields
        pName p;
        Uname U;
        //// Density
        //rho rhoInf;
        rhoInf 1.205;

        //// Centre of rotation
        CofR (0 0 0);
    }
////////////////////////////////////////////////////////////////////////////
////////////////////////////////////////////////////////////////////////////
    forceCoeffs_object
    {
        // rhoInf - reference density
        // CofR - Centre of rotation
        // dragDir - Direction of drag coefficient
        // liftDir - Direction of lift coefficient
```

```
        // pitchAxis - Pitching moment axis
        // magUinf - free stream velocity magnitude
        // lRef - reference length
        // Aref - reference area
        type forceCoeffs;
        functionObjectLibs ("libforces.so");
        patches (cylinder);
        pName p;
        Uname U;
        //rho rhoInf;
        rhoInf 1.205;
        //// Dump to file
        log true;
        CofR (0.0 0 0);
        liftDir (0 1 0);
        dragDir (1 0 0);
        pitchAxis (0 0 1);
        magUInf 1.0314e+02;
        lRef 0.01;       // reference length for moments
        Aref 0.0002;     // reference area 1 for 2d // for D=0.02
      writeControl   timeStep;
      writeInterval  1;
   }
////////////////////////////////////////////////////////////////////////
////////////////////////////////////////////////////////////////////////
   minmaxdomain
   {
        type fieldMinMax;
        functionObjectLibs ("libfieldFunctionObjects.so");
```

```
        enabled true;
        mode component;
        writeControl timeStep;
        writeInterval 1;
        log true;
        fields (p U T);
    }
    #includeFunc probes
////////////////////////////////////////////////////////////////////////////
}
```

BIOGRAPHY

NAME	Thanakorn Chanthanasaro
DATE OF BIRTH	December 23, 1992
PLACE OF BIRTH	Chanthaburi, Thailand
INSTITUTIONS ATTENDED	Mahidol University, 2010-2014 Bachelor of Science (Physics) Mahidol University, 2015-2020 Master of Science (Physics)
SCHOLARSHIP RECIEVED	Development and Promotion of Science and Technology Talents Project (DPST)
HOME ADDRESS	101/179 Moo 10, Tambon Thachang, Mueang, Chanthaburi, 22000, Thailand
E-MAIL	tc.phy.5g@gmail.com